JOURNAL OF GEOPHYSICAL RESEARCH, VOL. 111, B11308, doi:10.1029/2005JB004097, 2006

Three-dimensional dense strong motion waveform inversion for the rupture process of the 1999 Chi-Chi, Taiwan, earthquake

Shiann-Jong Lee,[1] Kuo-Fong Ma,[2] and How-Wei Chen[2]

Received 9 October 2005; revised 31 July 2006; accepted 16 August 2006; published 22 November 2006.

[1] We inverted the high-resolution spatiotemporal slip distribution of the 21 September 1999 Chi-Chi, Taiwan, earthquake utilizing data from densely distributed island-wide strong motion stations for a three-dimensional (3-D) fault geometry, and 3-D Green's functions calculations based upon parallel nonnegative least squares inversion. The 3-D fault geometry, consistent with high-resolution reflection profile, is determined from GPS inversion and aftershocks distribution. This 3-D fault model presents the dip angle gradually becoming shallower from south to north along the fault and near flat at the deeper portion of the fault. The 3-D Green's functions are calculated through numerical wavefield simulation from three-dimensional heterogeneous velocity structure derived from tomography studies. The Green's functions show significant azimuthal variations and suggest the necessity of lateral heterogeneity in velocity structure. Considering complex fault geometry and Green's functions in full 3-D scale, we invert the spatial/temporal slip distribution of the 1999 Chi-Chi earthquake using the best available and most densely populated strong motion waveform data. We perform the inversion under a parallel environment utilizing multiple-time window to manage the large data volume and source parameters. Results indicate that most slip occurred at the shallower portion of the fault above the decollement. Two major asperities are found, one in the middle of the fault and another one at the northern portion of the fault near the bend in the fault trace. The slip in the southern portion of the fault shows a relatively low slip rate with longer time duration, while the slip in the northern portion of the fault shows a large slip rate with shorter time duration. The synthetics explain the observations well for the island-wide distributed strong motion stations. This comprehensive study emphasizes the importance of realistic fault geometry, 3-D Green's functions, and parallel inversion technique in correctly accounting for both the detailed source rupture process and its relationship with the strong ground motion of this intense earthquake.

Citation: Lee, S.-J., K.-F. Ma, and H.-W. Chen (2006), Three-dimensional dense strong motion waveform inversion for the rupture process of the 1999 Chi-Chi, Taiwan, earthquake, *J. Geophys. Res.*, *111*, B11308, doi:10.1029/2005JB004097.

1. Introduction

[2] The 21 September 1999 (0147:12 LT, UT+8) Chi-Chi earthquake (M_w = 7.6) was one of the most destructive earthquakes in Taiwan during the past 100 years. Fault movement during the earthquake was interpreted as reverse, left-lateral faulting on a low-angle plane along the Chelungpu fault, characterized by a long rupture length (over 80 km) and long duration of about 30 s [*Ma et al.*, 1999]. A characteristic of the fault trace was a turn bending to the northeast at its northern tip, where the largest surface rupture was measured, 9.8 m horizontally and 5.6 m vertically. Complicated surface breaks, relative small amounts of slip in the south in contract to large slip in the northern portion of the fault all indicate the complexity of the fault rupture, which we believe is related to nonplanar fault geometry.

[3] A thin-skinned thrust model had been considered to explain the tectonic mechanism and fault geometry of the Chi-Chi earthquake [*Wang et al.*, 2000]. There is a decollement surface ranging in depth from 10 to 20 km, formed by the lithologic contrast of a weak layer with rock formation consisting of shale and sandstone layers. This surface has a slope of about 8 degrees, which matches the uplift of the basement high, forming a wedge type overthrusting. The nucleation point of Chi-Chi earthquake was situated on a fault plane that branched from the decollement, but was ramp-bend folded, and then followed a weak layer of Chinshui Shale until exposed at the surface. This model implies that the fault dip is gentler at the deeper part of the Chelungpu fault.

[4] Spatial slip distributions of the Chi-Chi earthquake have been investigated by other researchers. *Lee and Ma* [2000] used teleseismic broadband data to invert the rupture process. *Yu et al.* [2000] studied the coseismic surface

[1]Institute of Earth Sciences, Academia Sinica, Nankang, Taipei, Taiwan.
[2]Institute of Geophysics, National Central University, Jung-Li, Taiwan.

0148-0227/06/2005JB004097$09.00

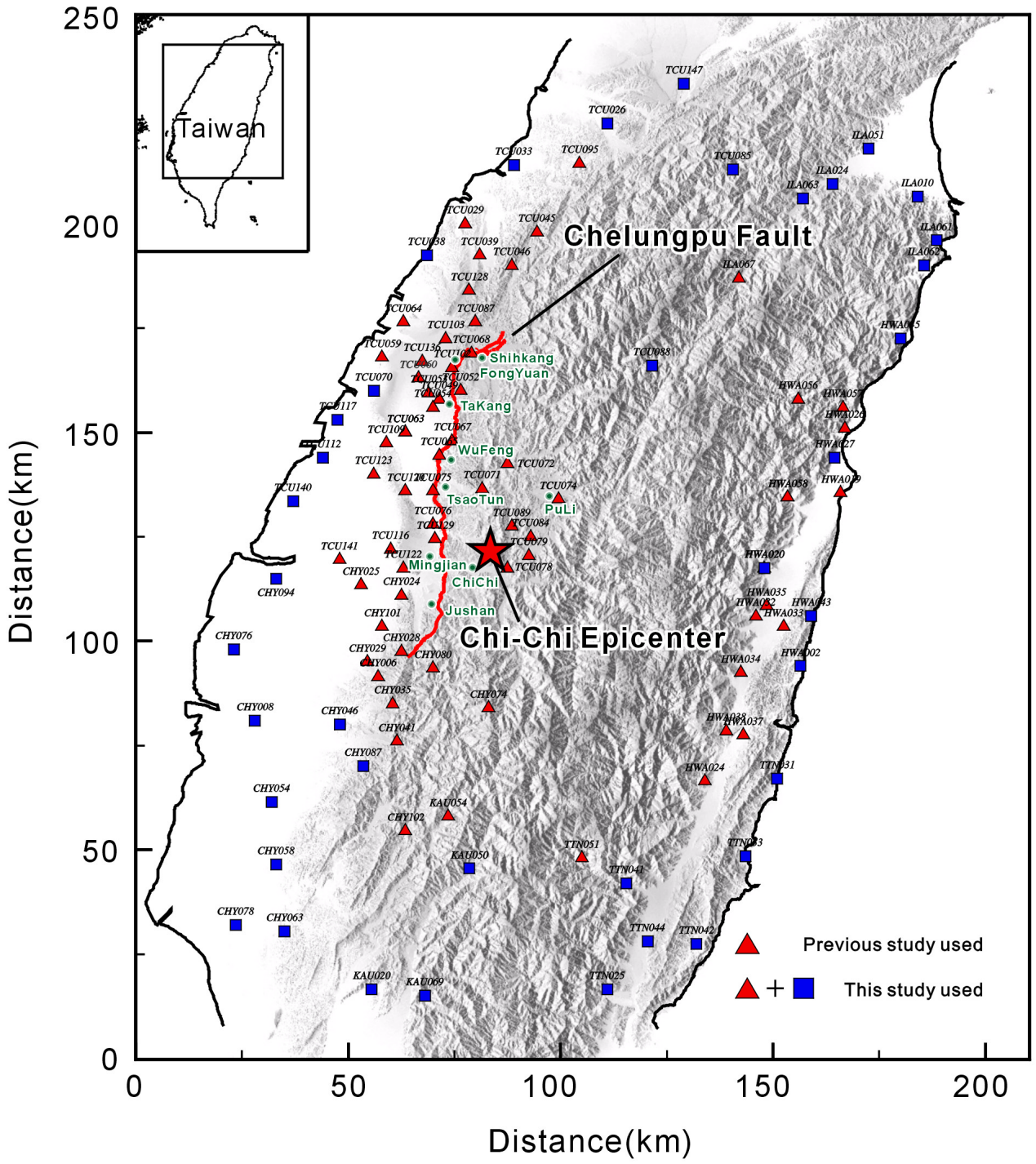

Figure 1. Strong motion station distribution used in the study. Red line shows the surface break during the Chi-Chi earthquake. The stations are separated into two groups. Triangles show the records used in the previous study which contain 63 strong motion stations. The second data set (squares) contain 40 stations which had larger epicenter distance and the azimuth coverage around the source area well. Also shown are the local towns around the source region.

displacement associated with the earthquake. *Zeng and Chen* [2001] analyzed both GPS and strong motion records to reveal slip distributions. *Ma et al.* [2001] combined strong motion, teleseismic and GPS data to investigate the spatial and temporal distribution of slip for the earthquake. All studies consistently show a large asperity existing at the north of the fault. In these studies, the use of strong motion records were very limited only covering a small portion of the dense data set. Furthermore, the fault models were hypothesized as single or segmented fault planes to explain the complex surface break of the Chelungpu fault. However, because the near source strong motion records are very

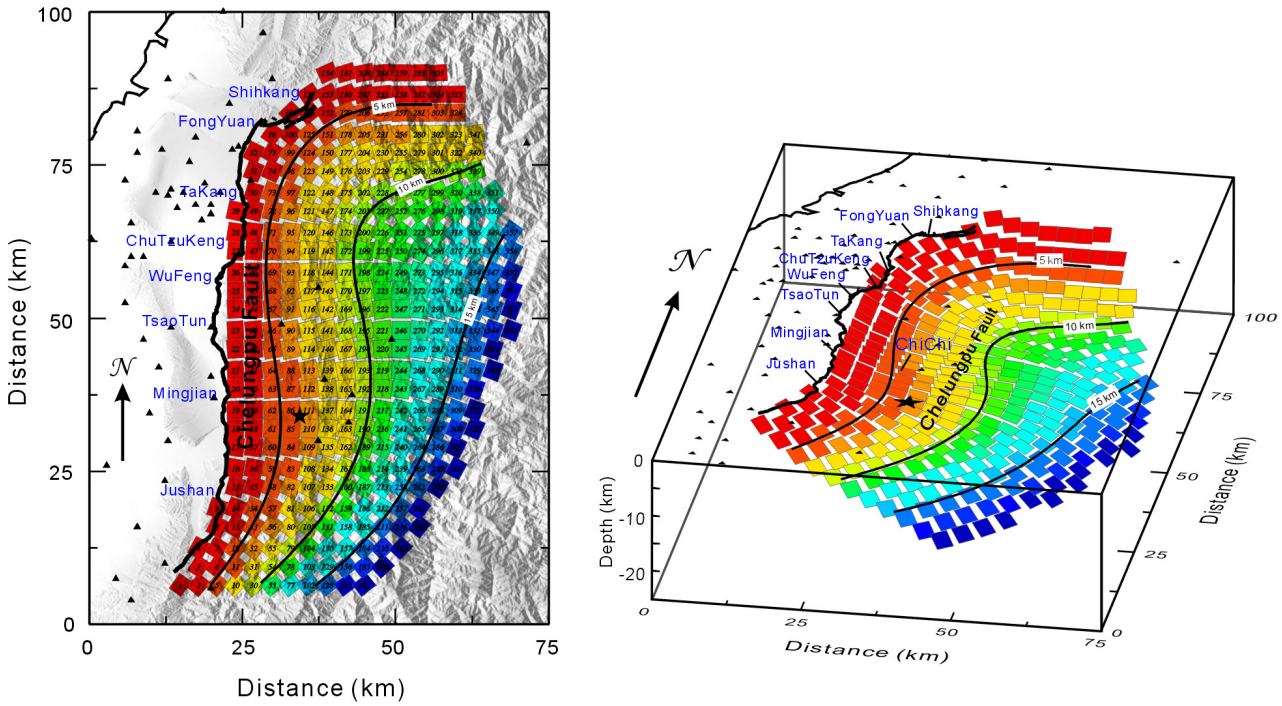

Figure 2. The 3-D trend surface fault models of the Chelungpu fault. (left) Map view according with the surface break (solid line), isodepth lines, epicenter (asterisk), strong motion stations (triangles) and the background topography. Numbers on each subfault indicate the subfault no. used in the inversion. (right) A perspective view of the fault plane from south border. Solid lines indicate the surface break and isodepth line on the fault plane. Also shown are the local towns along the surface break. A rainbow color scale is used to show the subfaults at specific depths in both diagrams.

sensitive to the local fault geometry, the inconsistency of the strong motion records for the stations close to the fault still exists [*Ma et al.*, 2001]. *Ji et al.* [2001] inverted both the static displacement from near source acceleration data and GPS data assuming layered subsurface structure. Their results showed good consistency between GPS data and strong motion static displacements. At the same time, the strong motion data they used were also limited and the fault model was based on a segmented fault without the variation in dip angle. Seismic surveys and geological evidences [*Wang et al.*, 2000] showed that the dip angle of the fault becomes shallow toward the north and also becomes flat at depth. It is proved that with limited data usage and over simplified fault geometry might yield some overestimated slip distribution at deeper parts of the fault [*Lee et al.*, 2006]. In addition, the timing problem of the strong motion record has never been considered in all previous source studies. Therefore the effect of the timing error on the inversion result must be examined.

[5] In this study, we attempt to eliminate the previous problems by improving data coverage and investigating important inversion issues by considering (1) the maximum available 131 island-wide strong motion stations immediately surrounding the rupture region with all three component records; (2) three-dimensional fault geometry; (3) three-dimensional Green's functions calculation to include complicated lateral variation three-dimensional (3-D) velocity structure; (4) extra consideration given for optimal multiple-time window; (5) absolute timings for both Green's functions and observations; (6) a parallel nonnegative least squares inversion scheme to deal with the large requirement of computing memory from having expended the optimal number of time windows. As a result of optimizing the time window requirement, the rupture delay time, slip duration time and related source parameters can be more accurately analyzed to resolve the detailed rupture process of the 1999 Chi-Chi earthquake.

2. Data and Method

2.1. Data

[6] The Central Weather Bureau (CWB) has an extensive strong motion data set for both the main shock and aftershocks of the 1999 Chi-Chi, Taiwan, earthquake sequence. For the main shock, 441 digital strong motion records were prepared and processed from 663 triggered data files. This data set is important for both seismology and earthquake engineering because it includes over 60 recording sites within 20 km of the fault ruptures for an Mw 7.6 event, which provides a fivefold increase of such near-field records so far available for the entire world. In this study, the free-field strong motion data from the Chi-Chi earthquake is obtained from the attached CD in a *Bulletin of the Seismological Society of America* dedicated issue on the Chi-Chi earthquake. The absolute timing and base line drift were corrected if necessary. This new updated data provides important constraints in timing during the inversion for spatiotemporal slip distribution. Figure 1 shows the distribution of stations used in this study. Overall station sites are

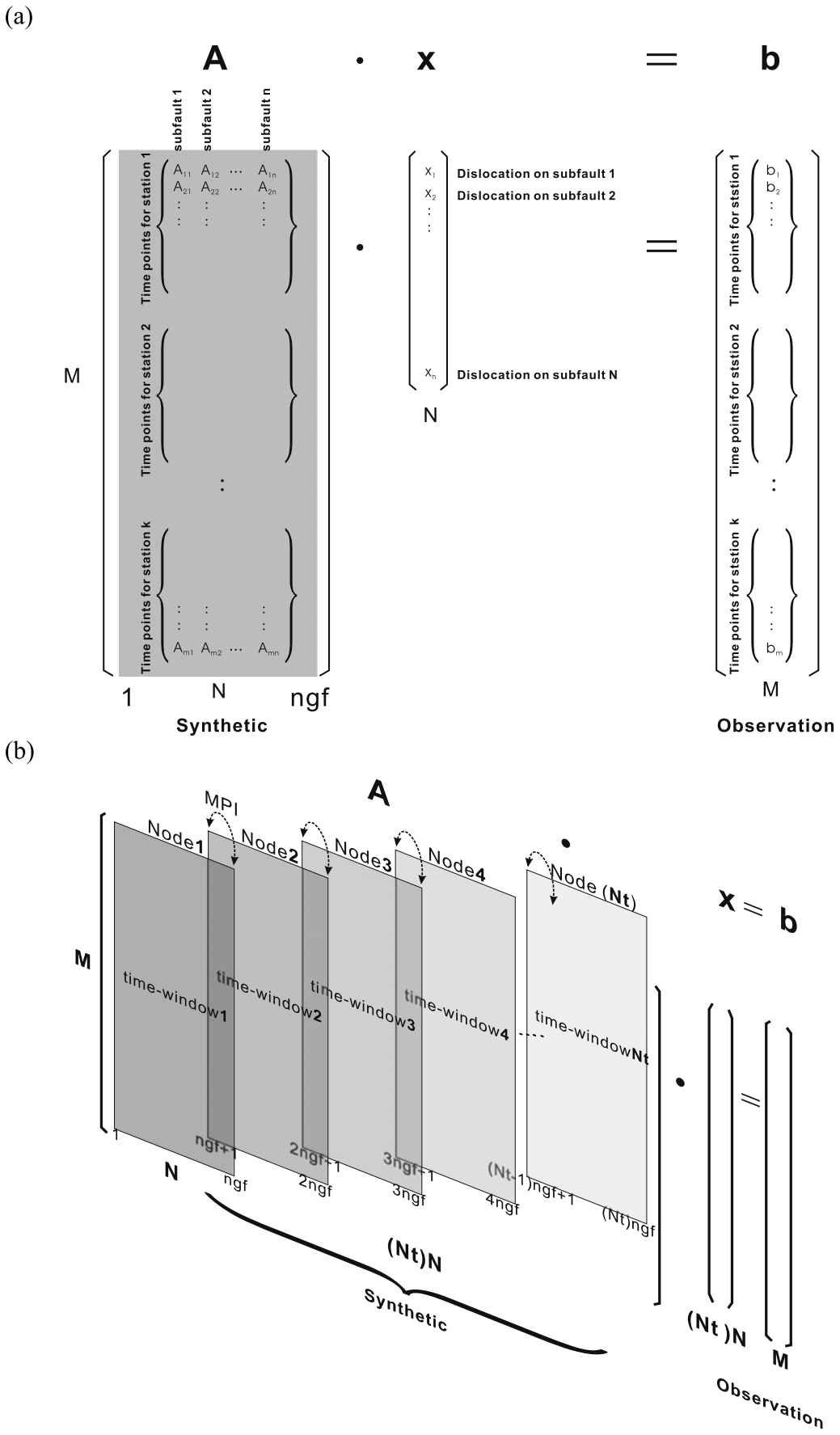
(a)
A
x
b
subfault 1
subfault 2
subfault n
Time points for station 1
Time points for station 2
Time points for station k
Dislocation on subfault 1
Dislocation on subfault 2
Dislocation on subfault N
Time points for ststion 1
Time points for ststion 2
Time points for ststion k
M
N
1
ngf
Synthetic
Observation
(b)
MPI
Node1
Node2
Node3
Node4
Node (Nt)
time-window1
time-window2
time-window3
time-window4
time-windowNt
ngf+1
2ngf+1
3ngf+1
(Nt-1)ngf+1
2ngf
3ngf
4ngf
(Nt)ngf
(Nt)N
(Nt)N

Figure 3

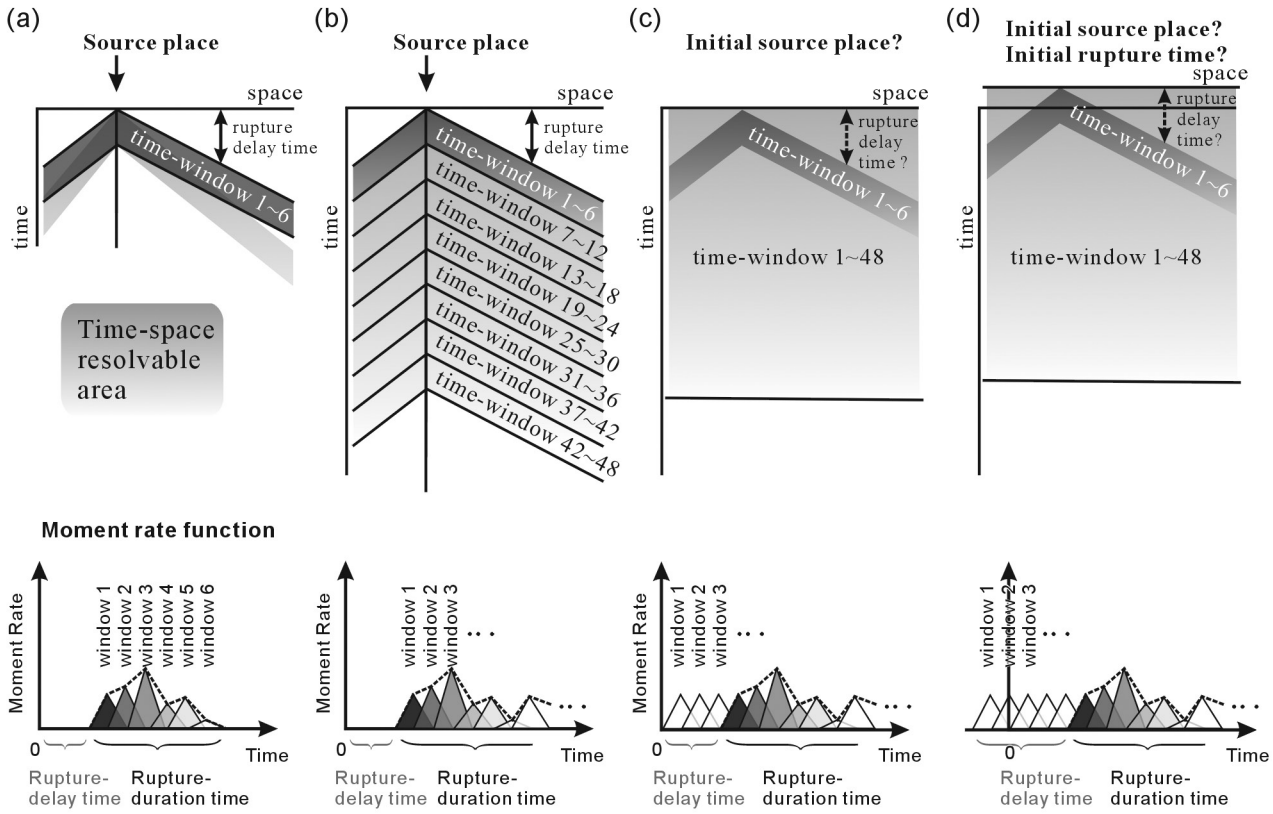

Figure 4. Solvable time-space range under different inversion implement. (a) Ordinary solvable range (used six time windows as the example); (b) parallel linear inversion with initial rupture velocity assumed; (c) parallel linear inversion without initial rupture velocity assumed (zero rupture delay time); (d) parallel linear inversion without initial rupture velocity assumed and shift the time of the Green's function. (bottom) Diagrams of the solvable moment rate function for each condition. By applying the parallel NNLS scheme, the inverted parameters can cover all spatiotemporal unknowns and thus becomes a full time-space inversion.

classified as A and B [*Lee et al.*, 2001]. To compare the inversion result to previous studies [*Ma et al.*, 2001; *Zeng and Chen*, 2001; *Wu et al.*, 2001; *Ji et al.*, 2001], all of the stations used in the published work of 63 strong motion stations are considered. An additional 40 stations, which have larger epicenter distance and better azimuth coverage around the source area, are used in order to obtain the highest resolution possible for our inversion. In sum, 103 three-component stations yield a total of 309 records are included in this study.

2.2. The 3-D Fault Model and 3-D Green's Functions Calculation

[7] The 3-D fault geometry is established by surface fault trace and 327 relocated aftershocks by means of trend surface analysis [*Lee et al.*, 2006] (Figure 2). The attitude of the Chi-Ch fault plane is inferred from focal mechanisms of main shock and several aftershocks, direct outcrop measurements and the near fault drilling data. The calculation from surface break slip data is used to check the accuracy of the result of trend surface. For such a complex fault model, the strike and dip vary at different position of the fault. Two obvious characteristics can be found in this fault model. The first shows that the strike is rotated from a north-south direction to a northeast direction, especially at the northern end. The second characteristic indicates that the dip angle become less steep, from 30 degree at shallow depth to about 7–8 degrees at the deeper portion of the fault, corresponding to the thin-skinned thrust model as described by *Wang et al.* [2000]. These characteristics are applied to the 3-D fault model to help avoid possible pseudoslip on the fault plane, especially for the near fault stations, which are sensitive to the fault geometry. We give each subfault with a length and downdip width of 3 km in a finite fault approach. The total number of subfaults in the 3-D trend surface fault model is 357. Each subfault has a point source at the center, according to the strike and dipping angle on the fault plane so that each subfault has different

Figure 3. System of linear equation $\mathbf{Ax} = \mathbf{b}$. (a) Traditional single time window matrix system where $\mathbf{A}$ is the matrix of synthetic waveforms, $\mathbf{b}$ is the observed data vector, and $\mathbf{x}$ is the solution vector of the slip on each subfault. (b) Multiple-time window with matrix decompose in the parallel NNLS inversion. Message Passing Interface is applied as the communicant between the computing nodes in the parallel computing process.

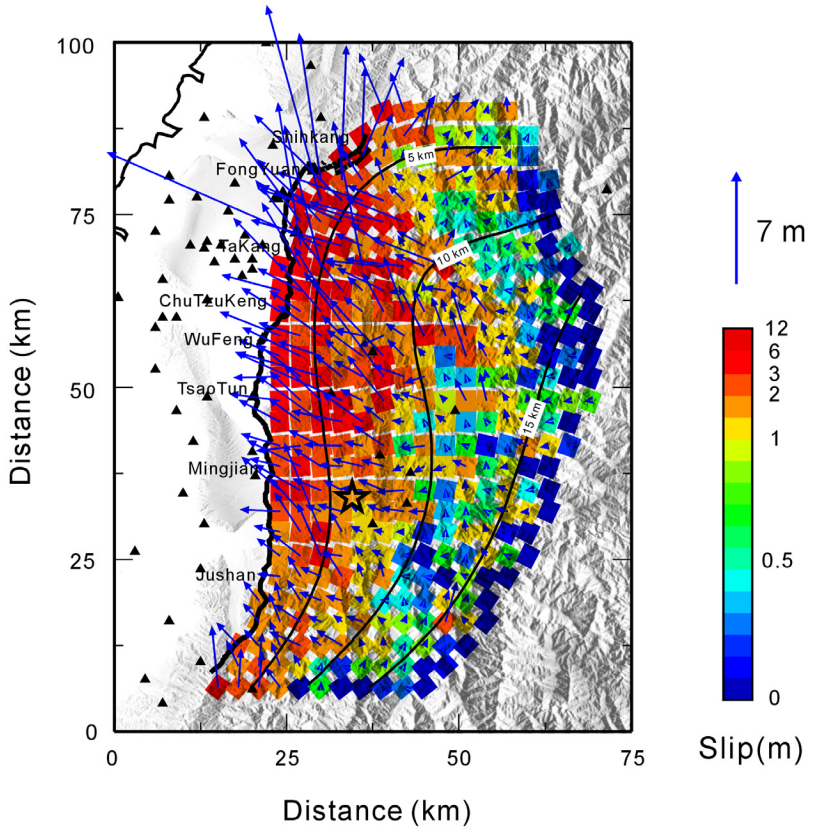

Figure 5. Total slip distribution and slip vectors over the fault plane. The amount of slip is indicated by shading as shown in the legend. The arrows indicate the slip vector on the rupture plane.

strike and dip. The average rake angle during the Chi-Chi earthquake is about 66°, thus we consider two components in the inversion: rake 20° and rake 120°. Finally, the rake angle on each subfault is varied within a reasonable range determined by inversion parameters.

[8] To account for the influence of lateral wave propagation effect, we compute three-dimensional Green's functions using a finite difference method. To avoid the artificial reflection coming from the model boundary, we adopt a composite boundary comprising A_2 boundary condition [*Clayton and Engquist*, 1977] and nonreflection boundary condition [*Cerjan et al.*, 1985]. The large-scale 3-D velocity model is derived from the tomography inversion result of Taiwan [*Rau and Wu*, 1995]. *Lee and Chen* [2000] have found that this tomography model provides more evident 3-D traveltime characteristics than 1-D layered model [*Ho and Shin*, 1994] and other tomography inversion results [*Roecker*, 1987; *Ma et al.*, 1996]. A forward simulation test on 1-D and 3-D velocity models is given in Appendix A. The analysis shows that the tectonic settings within Taiwan would have an evident influence on seismic wave propagation in both traveltime and waveform. The results as shown in Appendix B also indicate that an accurate description of Green's functions, especially when the known tectonic settings are complex, may considerably affect the inversion results. The complexities of 3-D continental structure cannot be ignored and is necessary to be considered in the Green's functions. For the purpose of numerical analysis, the velocity model is then divided into 0.5 km interval grids. Owing to the resolution of the 3-D topography model, the frequency band of the calculated Green's function is constrained under 0.5 Hz. Taking account of low-frequency and large-scale 3-D wave propagation simulation, a second-order finite difference scheme is used to provide stability with reasonable calculation time.

2.3. Parallel Nonnegative Least Squares Inversion

[9] The observed and synthetic Green's functions are formulated as a system of linear equation:

$$\mathbf{A}\,\mathbf{x} = \mathbf{b}, \tag{1}$$

where **A** is the matrix of synthetic waveforms, **b** is the observed data vector, and **x** is the solution vector of the slip on each subfault. This linear equation system is shown in Figure 3a. Each column of **A** is composed of the Green's functions, strung end to end, for a particular subfault and a particular mechanism (rake 20° and rake 120°) for all the stations in the inversion. Similarly, **b** is formed by stringing of all observation records end to end. Hence each time point on each record is explicitly included in the inversion. The number of columns of **A** depended on the number of elements on **x**. To allow the variation in rake, the elements of **x** consist of two rake angle components on each subfault. Accordingly, the Green's functions in matrix **A** are also calculated for the two components, respectively. We solved equation (1) using nonnegative constraints of linear least squares. To make the inversion result stable, the damping,

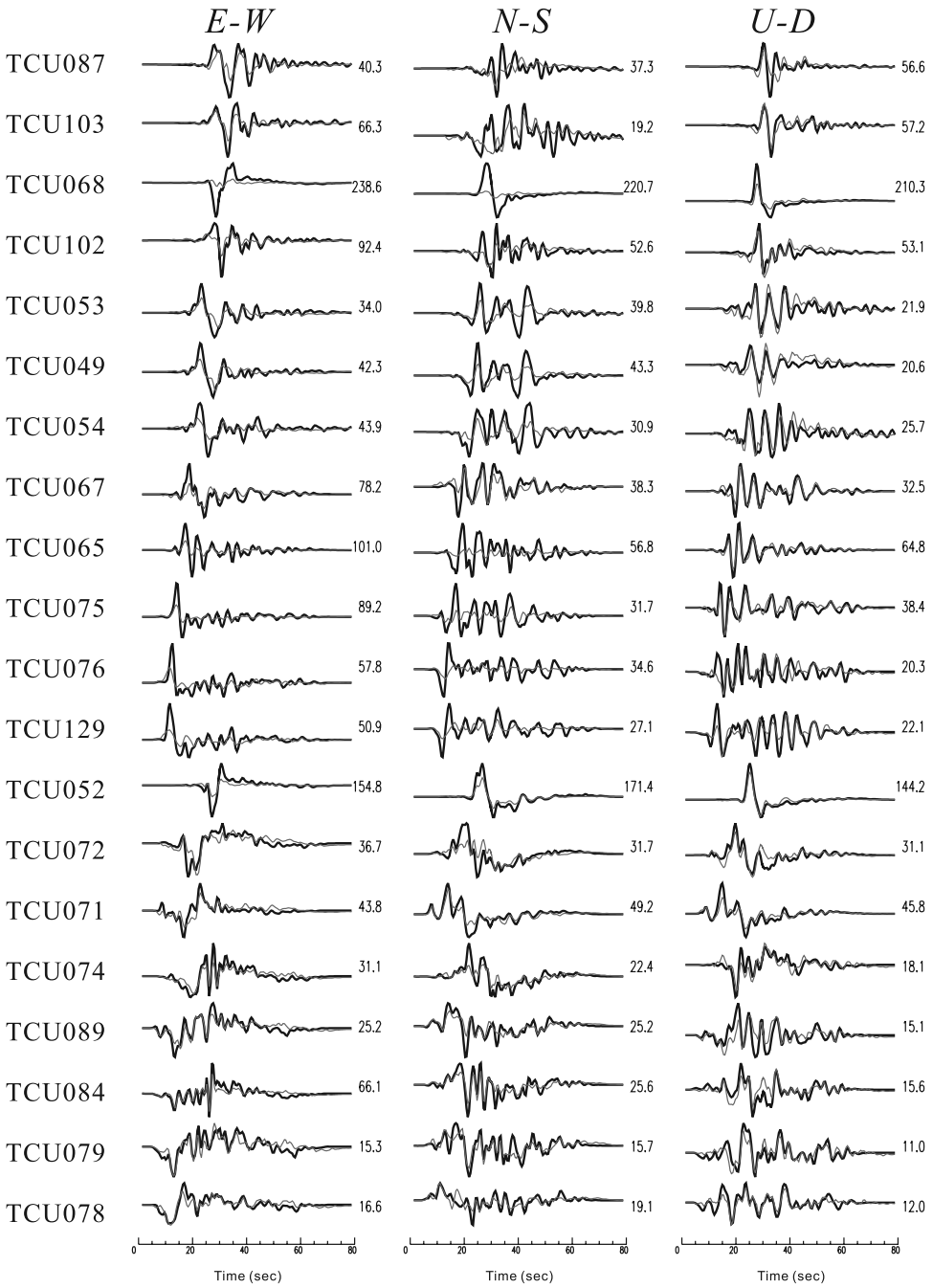

Figure 6. Comparisons of the synthetics (red thin lines) and observations (black thick lines) for the stations at (a) near source region; (b) western side of the surface break; (c) eastern side of the fault; (d) northern region of the fault; and (e) southern region of the fault. Each row shows the component of E-W, N-S and U-D, respectively. The waveforms in the same column represent the observed and synthetic for the same station. The numbers next to the seismograms show the peak velocity amplitude of the observed records.

smoothing and minimum solution constraints are considered under different situations. Other stability constraints have been discussed by *Hartzell and Heaton* [1983]. This inversion method as we applied in the study has successfully been used in analyzing the slip distribution and rupture processes of many large earthquakes, e.g., the 1983 Imperial Valley, California, earthquake [*Hartzell and Heaton*, 1983], the 1992 Landers, California, earthquake [*Wald and Heaton*, 1994], and the 1994 Northridge, California, earthquake [*Wald et al.*, 1996].

[10] For large earthquakes, source time functions are usually varied within the fault. To simulate the complex source time functions, a multiple-time window is necessary in the inversion. In this situation, matrix **A** is then formed by *Nt* time windows side by side and vector **b** becomes *Nt* times the single time window where *Nt* is the number of

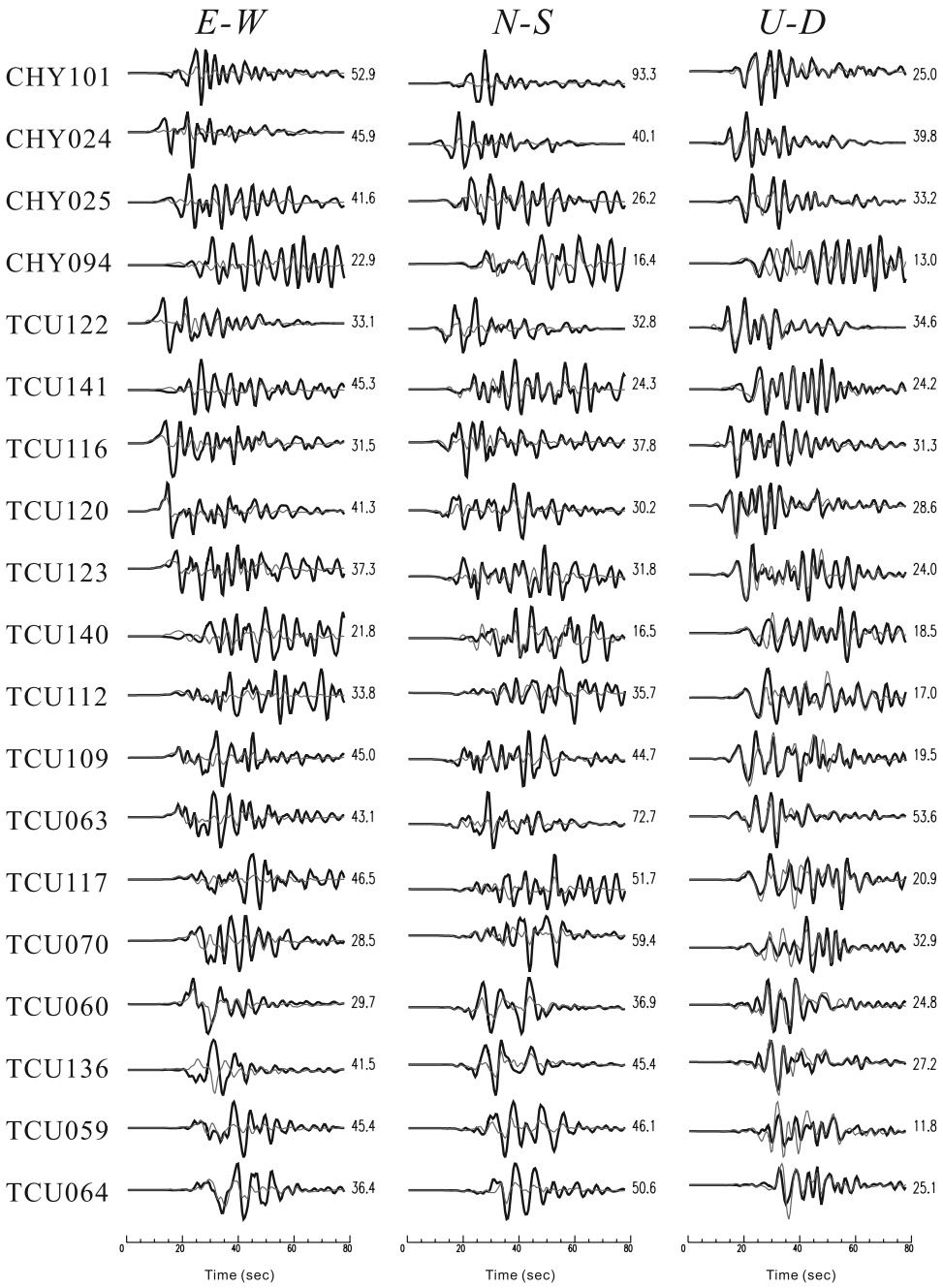

Figure 6. (continued)

windows. Furthermore, rupture velocity is also an important parameter which must be assumed before the inversion. All the slip on the fault must be initiated after the rupture front passes through, namely the rupture delay time, followed by the source duration time. We consider the multiple-time window and rupture delay time varied under a certain range after the initial assumption. In the multiple-time window analysis, we allowed each subfault to slip in any one of 2.0 s time windows following the passage of the rupture front. Each window had an overlap of 1.0 s. If the slip occurs at a later time window, its characteristic rupture delay time will be longer. In other words, the rupture velocity in that area will be relatively slow. Under the multiple-time window condition, the source time function and rupture velocity in the inversion could be more flexible and resulting in more reliable results.

[11] Multiple-time window can provide more reliable results. However, an increase in the number of time windows would results in a large expansion of matrix **A**. For a source duration of more than 15 s [*Ma et al.*, 2001], the Green's functions of 2 s with 1 s overlap and at least 14 time windows are required leading to a large demand for computing capacity to perform the calculations. To solve this problem, we develop a parallel nonnegative least squares (parallel nonnegative least squares (NNLS)) inversion program which essentially decomposes matrix **A** into present

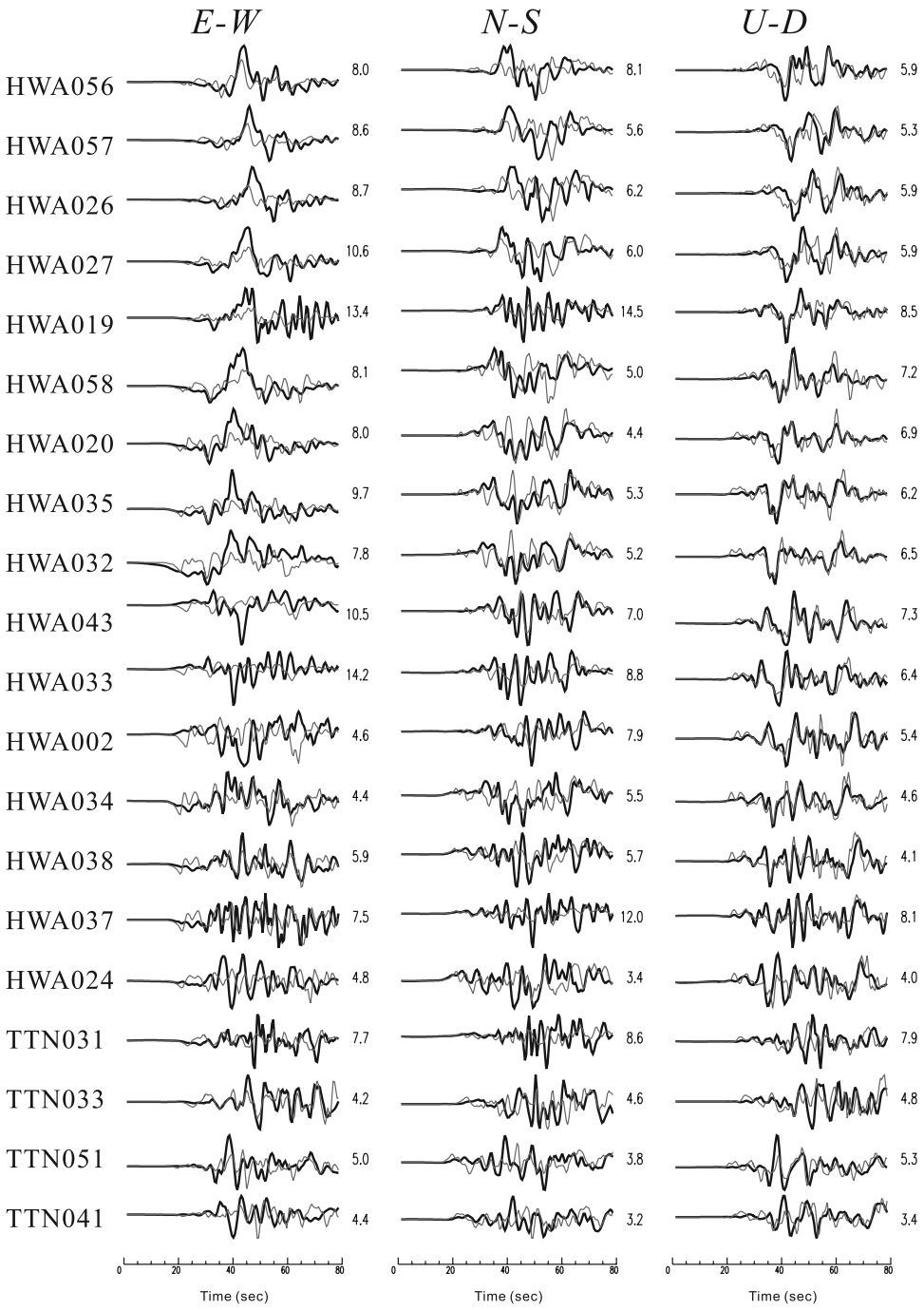

Figure 6. (continued)

computing nodes, and thus improves the number of time windows and promotes program performance. Message Passing Interface (MPI [*Gropp et al.*, 1996]) is applied as the communicant between the computing nodes in the parallel computing process. Figure 3b is a diagram showing the setting of matrix decomposition in the parallel NNLS inversion. This allowance for more time window calculations gives better solvable time-space coverage and provides a compromise solution between high-frequency Green's functions and long local duration time on the subfault. The optimum capacity of our computer facility, using a parallel NNLS program, can solve at least 48 time windows under an 8-Node PC cluster. Figure 4 shows the solvable time-space range and the benefits of using parallel NNLS technique to invert spatiotemporal slip distribution compared with nontime window or limited time window inversion. By using the parallel NNLS scheme, allows for not only the number of time windows to be increased but also for some advance applications to be considered. Initially, we assume the rupture velocity as infinite with no

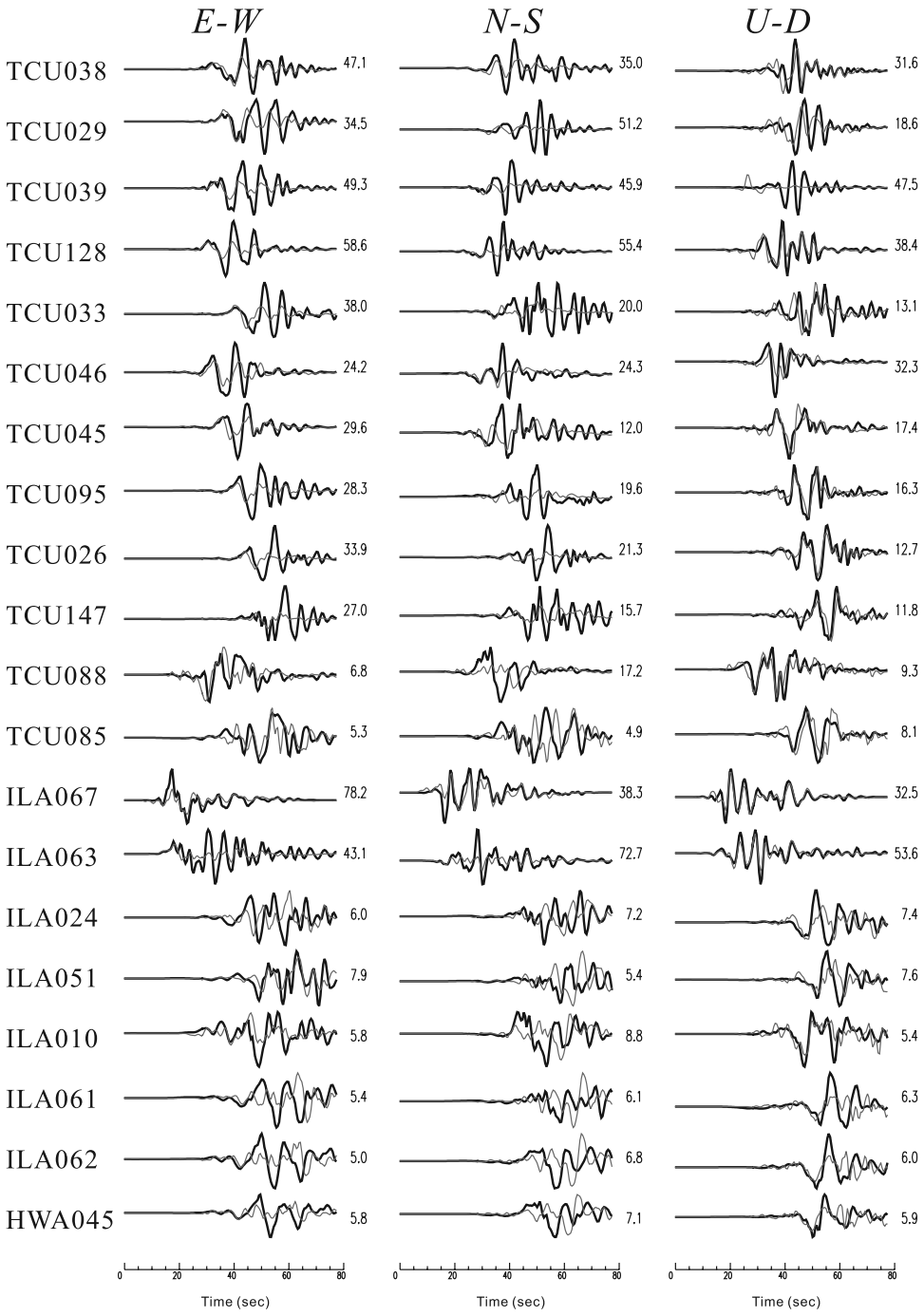

Figure 6. (continued)

rupture delay time and name it the ''zero rupture delay time'' approach (Figure 4c). By this assumption, a supersonic rupture can be considered and the position of the nucleation point can be redefined after the inversion. Furthermore, as we shift the time of the Green's function, the initial rupture time can also become the invertible parameter (Figure 4d). After these further applications by parallel NNLS technique, the range of inverted parameters covers all spatiotemporal unknowns during the rupture and thus becomes a full time-space inversion. A detail resolution tests on the stability and the necessity of extra multiple-time window is given in Appendix B.

3. Inversion Results

3.1. Spatial Distribution

[12] Because of the enhanced azimuthal coverage of these 103 stations, the inversion is carried out without smoothing. However, solution minimization is employed in the inversion because of the large number of time windows, potentially yielding a larger seismic moment. Thus solution minimization constraint plays an important role in the total

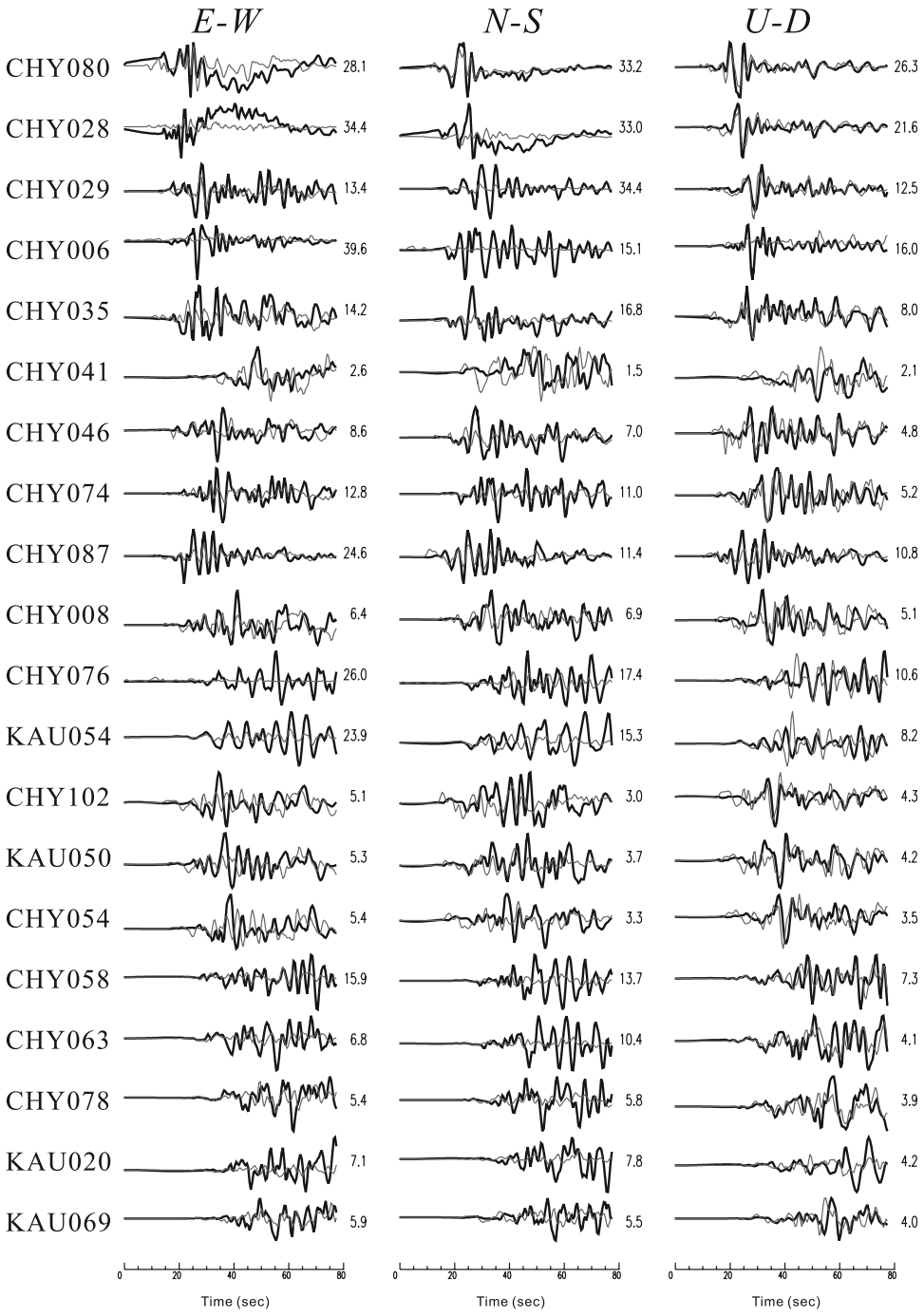

Figure 6. (continued)

moment and local slips. In general, a larger constraint on minimization reduces the amount of seismic moment but increases the data variance.

[13] Figure 5 shows the final inversion result derived from 48 time windows. From the isodepth line we can see that most of the slip is located at the shallow part (<10 km) of the fault, generally between the regions from hypocenter to free surface. This means that the Chi-Chi earthquake was nucleated at around 10 km deep branched from the decollement then rupture through the previous weak plane, Chelungpu fault, to the surface. This result is comparable with the thin-skinned thrust model as suggested by *Wang et al.* [2000]. The slip region at the southern part is concentrated in a narrow width of about 10 km with an average slip 2 m. The slip amount and width increase to the north, with a maximum slip of about 15.8 m, located at the bending of the fault (depth 4.5 km). This large slip region extends downward at least 10 km. It cuts through the Tachiah River at the free surface resulting in a spectacular 8 m high faulted waterfall. Note that the slip near the epicenter (about 1.5 m) compared to the slip in the northern region is relatively small. This phenomenon is often observed in similar source

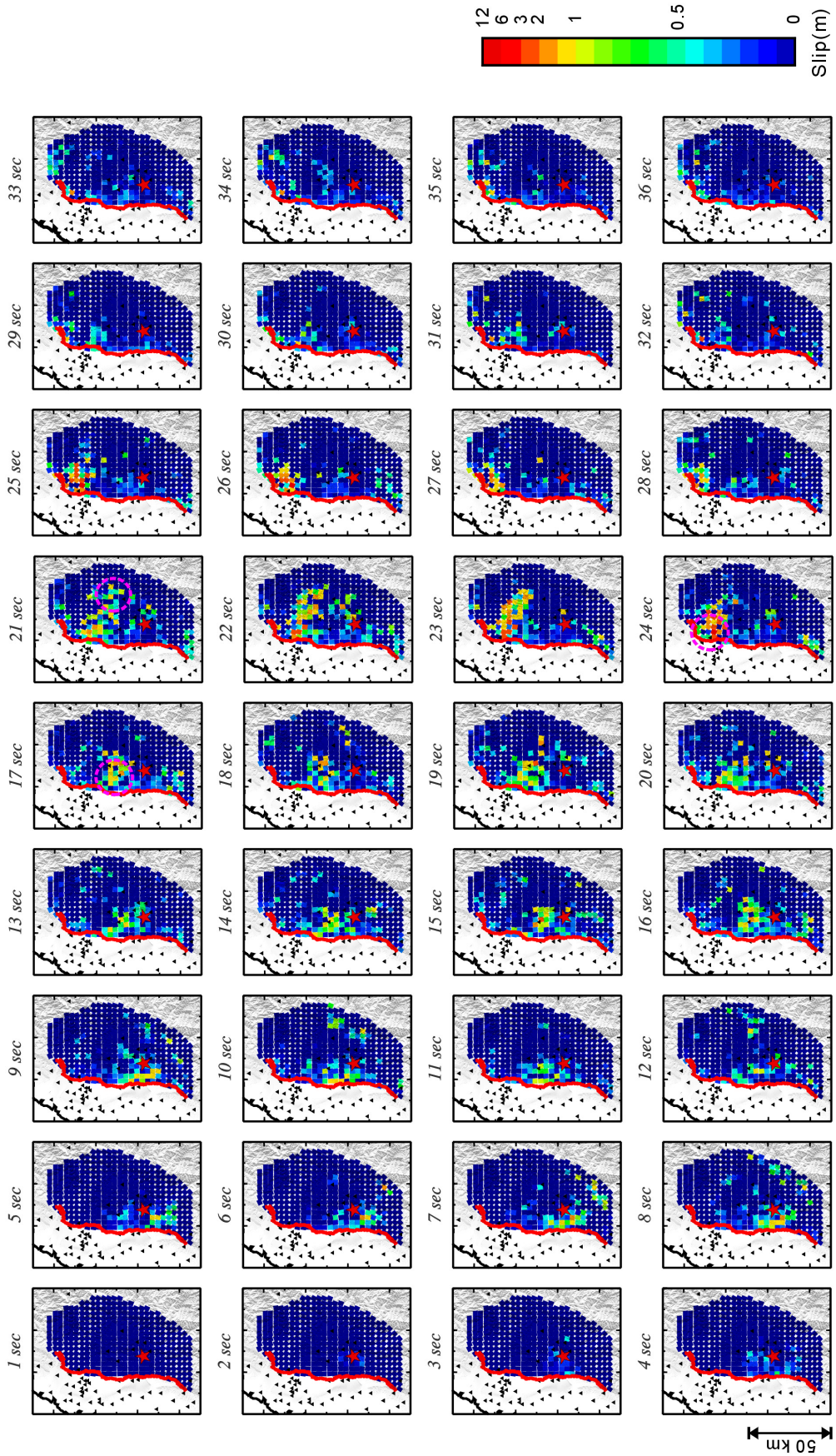
12
6
3
2
1
0.5
0
Slip(m)
1 sec
2 sec
3 sec
4 sec
5 sec
6 sec
7 sec
8 sec
9 sec
10 sec
11 sec
12 sec
13 sec
14 sec
15 sec
16 sec
17 sec
18 sec
19 sec
20 sec
21 sec
22 sec
23 sec
24 sec
25 sec
26 sec
27 sec
28 sec
29 sec
30 sec
31 sec
32 sec
33 sec
34 sec
35 sec
36 sec
50 km
50 km

Figure 7

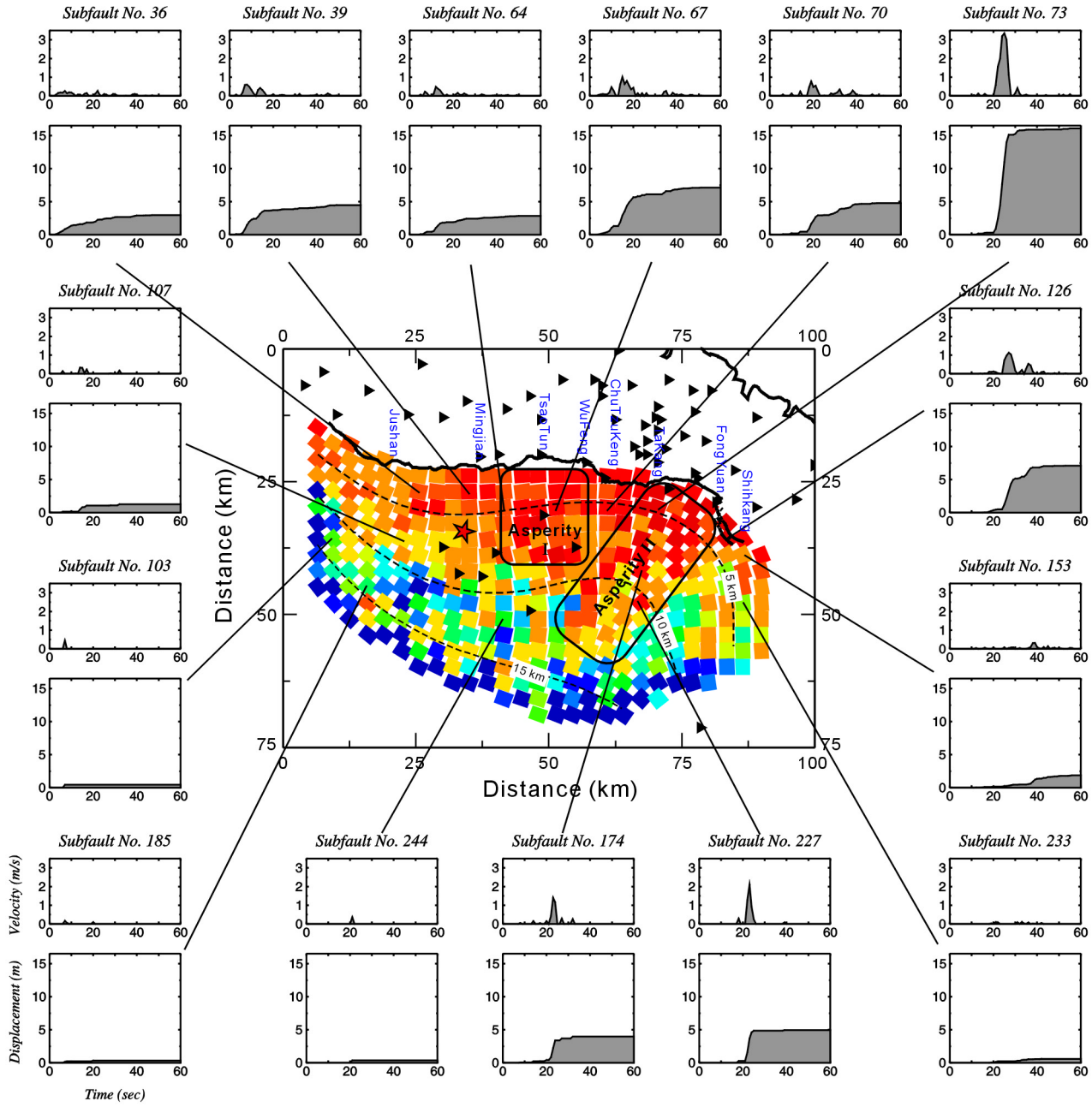

Figure 8. Comparison of slip behavior at different parts of the fault plane. The center sketch shows the total slip distribution on the fault plane. The others around the main panel show the slip velocity (top box) and accumulated slip (bottom box) with time at the corresponding subfaults.

studies of damaging earthquakes, i.e., slips near the epicenter are usually relatively small compare with asperity regions: such as the 1979 Imperial Valley earthquake [*Hartzell and Heaton*, 1983]; 1989 Loma Prieta earthquake [*Wald et al.*, 1991]; 1992 Landers earthquake [*Wald and Heaton*, 1994]. The slip below 10 km in depth is smaller compared to the shallower regions. Although this slip amount is not apparent, it still shows that the base decollement, where the dip angle of the Chelungpu fault becomes more flat, is involved in the Chi-Chi earthquake sequence.

[14] The vector in Figure 5 shows the rake angle on the fault plane during rupture. The average slip vector follows a

Figure 7. Rupture time history of Chi-Chi earthquake. The snapshots are taken at 1-s intervals. The open red circles at 17, 21, and 24 s are the positions of TsaoTun, PuLi, and FongYuan, respectively. Surface break (solid red line), epicenter (asterisk), strong motion stations (triangles) are also shown. The amount of slip is defined by the rainbow color scale as presented in the right legend.

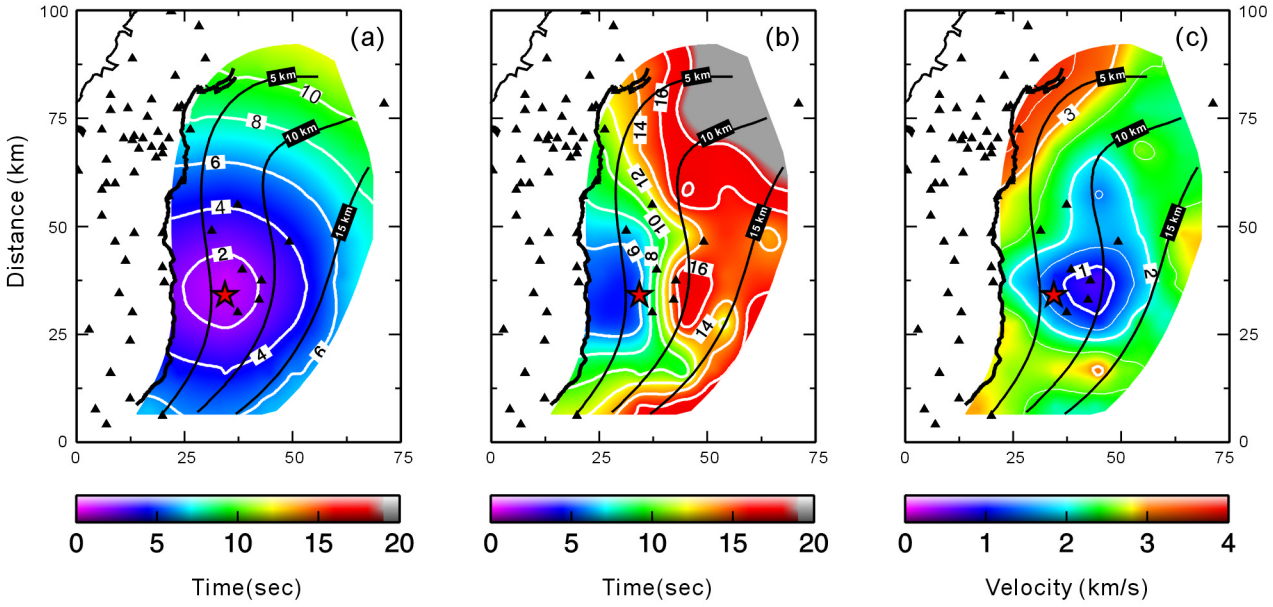

Figure 9. (a) Initial rupture delay time, (b) inverted rupture delay time, and (c) inverted rupture velocity. To determine the real rupture delay time after the inversion, we define the rupture front to have passed as the accumulated slip amplitude reaches 0.1 m on the subfault. The shortest distance from the initial rupture point to the subfault divided by the inverted rupture delay time is the localized rupture velocity.

NW-SE direction, which is similar to the result of Harvard centroid moment tensor (CMT) solution. However, in detail, the rake angle on each subfault has apparent variations. In the south and middle part of the Chelungpu fault, the average rake angle is 66°. While in the northern part, as the strike turn to northeast, the rake angle varies from 60° to 90° near the dip-slip mechanism. Some subfaults show rake angle larger than 90°, suggesting a right-lateral thrust slip. The rake angle on each subfault varies along the fault perhaps resulting from the strike on the 3-D fault geometry changing significantly. During rupture, the direction of the main stress is uniform around the rupture region, but the rake angles seem to change apparently on the fault plane as a result of the complex geometry of the Chelungpu fault.

[15] Figure 6 shows the comparison of the observed and synthetic three-component waveforms for the final inversion result. We represent our results by dividing the stations into five groups, A-E: (A) 20 stations in adjacent source region (B) 19 stations in western side of the fault, (C) 23 stations in eastern side of the fault, (D) 20 stations in northern part of the fault and (E) 21 stations in southern part of the fault. In general, the synthetic waveforms satisfy the observations in amplitude and frequency. The misfit, defined as $(\mathbf{Ax} - \mathbf{b})^2/\mathbf{b}^2$, is 0.70. Some simulated waveforms cannot fit the records well because the extreme amplification on the waveform, such as TCU068e, TCU068n and TCU052e which maybe due to the unaccounted for site irregularities. Otherwise, the synthetic for the U-D component in general explains the observation better than other components. This phenomenon maybe derived from the higher resolution tomography result in the Z direction and thus the Green's functions can fit the data more reasonably. Under different regions, the inversion results at the near source station give the best fit among all regions on vertical component. All three components in this region fit the data well. If the higher accuracy 3-D velocity model can be used for the calculation of the Green's functions, the misfit will certainly reduce.

3.2. Slip Time History

[16] Because of the constraints of the numerical technique, most source inversion studies can only consider short duration times with low-frequency source time functions. Even for quite recent source studies on the Chi-Chi earthquake, the longest invertible source duration time on local subfault is not more than 20 s [*Ma et al.*, 2001; *Zeng and Chen*, 2001; *Wu et al.*, 2001; *Ji et al.*, 2001]. By using a parallel linear inversion scheme in this study, a duration time of at least 50 s, with 1 s resolution, under 48 time windows on each subfault can be achieved, which can provide adequately complex source time functions and help to recover a high-resolution rupture processes. We assume a higher rupture velocity providing the maximum value as 5 km/s. Thus the phenomenon of supersonic rupture can be considered in the inversion. Although the parallel NNLS technique can help to invert the initial nucleation location and time by assuming zero rupture delay time, but according to the data quality constraint and related stability problems would be appeared during inversion, hence a nonzero rupture delay time assumption is used in this study. By considering an initial rupture velocity under the hypothesis of nonzero rupture delay time, the initial rupture location would remain at the Chi-Chi hypocenter. Figure 7 shows the rupture time history of the Chi-Chi earthquake derived from this study. At the beginning, the slip near the hypocenter is relatively weak. After 5 s, larger slip magnitude occurs at the southwest part of the hypocenter, and the rupture energy propagates northward. At 11 s, the rupture

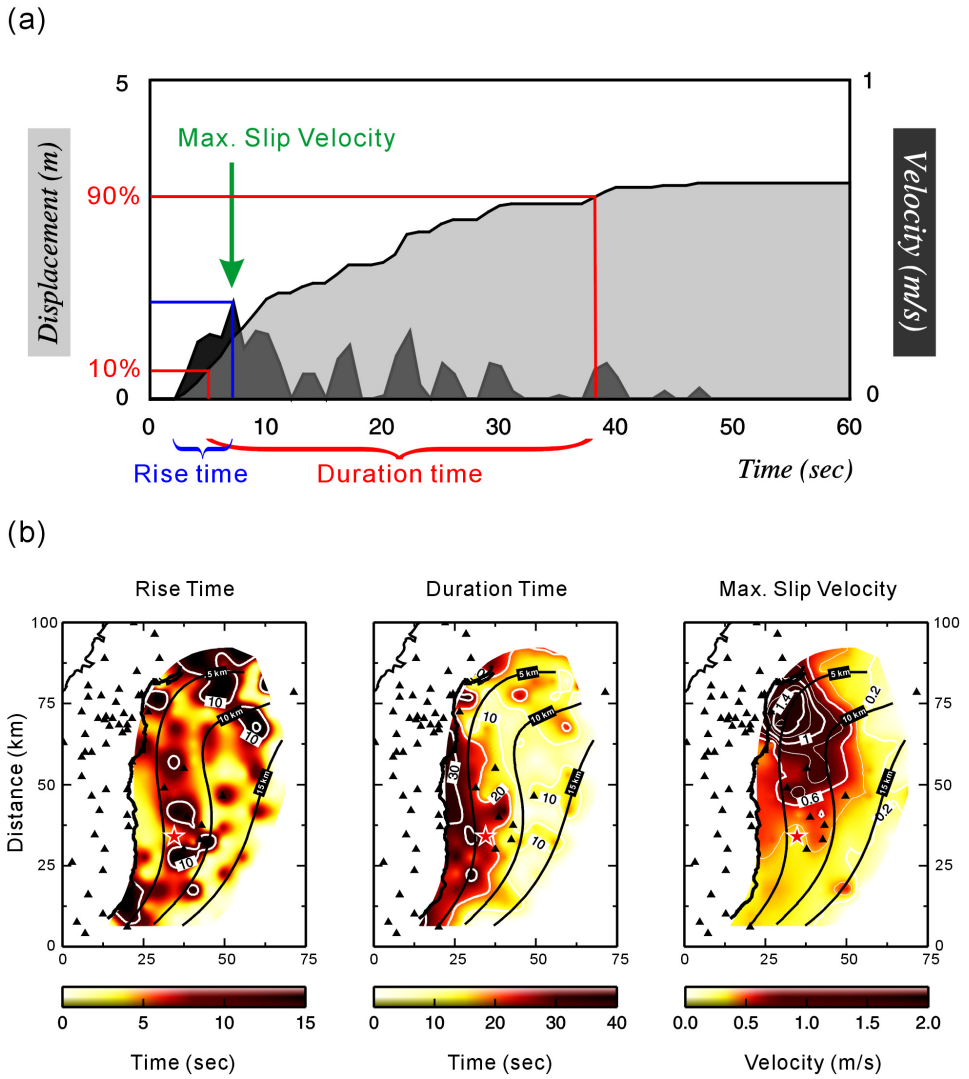

Figure 10. (a) Redefinitions of risetime, duration time, and maximum slip velocity used in this study. Subfault 36 is used as the example. The light gray area shows accumulated displacement on the subfault and the dark gray area shows the slip rate during the rupture process. (b) Distributions of redefined risetime, duration time, and maximum slip velocity on the fault plane.

front reaches the middle part of the fault plane, near the TsaoTun area, and both the rupture velocity and slip amplitude drop. No obvious variation happens until 17 s, the rupture region almost stops at the middle part of the fault, and the amount of slip increases slowly during this period. This phenomenon near the TsaoTun area might represents the first asperity on the Chelungpu fault. At 18 s, the rupture front overcomes the friction on the asperity, and releases large amounts of stress energy. Following that release, the rupture behavior becomes irremediable that quickly expands toward the north and east. The deeper part of the fault, under the northern PuLi basin, produces intense slip at 21 s. Then the rupture energy immediately propagates toward the shallower part in a northwest direction, forming a 25 km long by 10 km wide strong shaking zone. This is the second major asperity on the Chelungpu fault plane. The shaking energy from this intense rupture zone reaches the free surface at 24 s, joining the rupture at the shallow part, and producing large slip magnitude in the FongYuan area which resulted in the 8 m high faulting waterfall and destroyed the Shihkang dam. This damaging rupture behavior has a long duration time from 21 to 28 s. After 29 s, the slips on the fault gradually decrease, although there are still some small ruptures that propagate from middle to northern on the fault plane. Some weak slips occur at the eastern bending of the fault after 30 s. A few tiny slip events occur at the shallower part of the fault after 50 s. The overall active rupture behavior stops after 60 s.

3.3. Slip Time Function

[17] Rupture time history analysis indicates that the total slip duration on the Chelunpgu fault is about 60 s, which is two times longer than the results of previous studies of this sequence [*Ma et al.*, 2001; *Zeng and Chen*, 2001; *Wu et al.*, 2001; *Ji et al.*, 2001]. For detailed rupture behavior at different parts of the fault plane, we determine the possible rupture process for different scenarios through a high-resolution analysis. Figure 8 compares the slip velocity

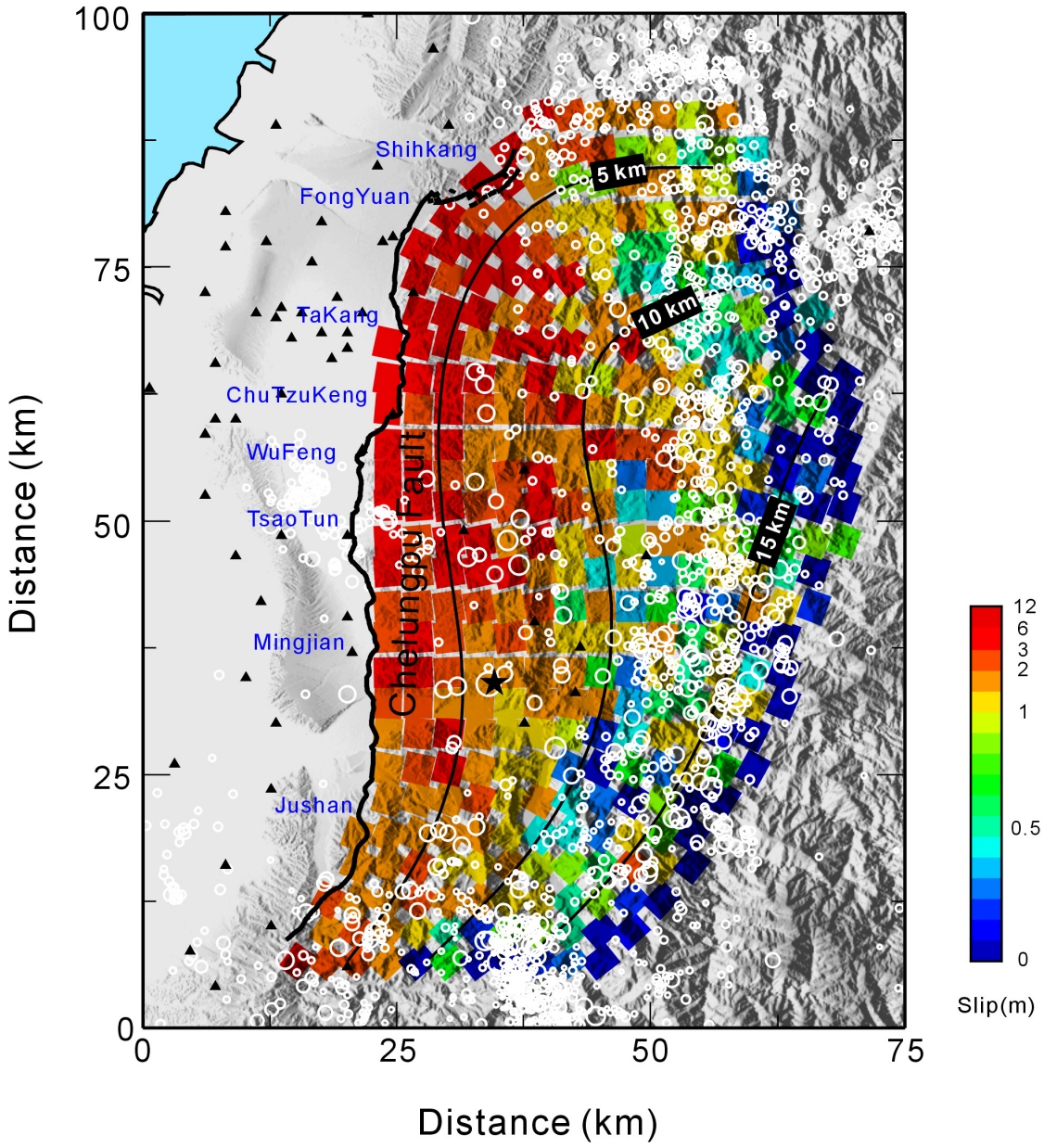

Figure 11. Comparison between inverted slip distribution and aftershocks (open circles). These aftershocks ($M_L > 1$) were recorded by CWB between 1999 September and 1999 November.

and slip amount with time at different parts of the fault plane. It shows that the rupture behavior on the fault is quite heterogeneous. First, we analyze subfaults near the surface break. The slip rate is small, with a short duration for the subfault at the southern part of the fault, while the slip repeats several times between 10 and 50 s. From the slip versus time diagram (Figure 8), it is obvious that total slip accumulated intermittently during time >30 s. In the middle part of the fault, the rupture is persisted for a majority of slip sequence. Note that long-period duration occurs a few seconds after the passing of the rupture front. This phenomenon indicates the first asperity near TsaoTun. When the rupture front reaches this region, the initial slip is very weak. As the rupture overcomes the barrier, large amounts of long-period energy are released. In short, for the slip along the surface rupture break, the more of the subfault near the northern end, the shorter of the total duration time with increasing slip rate. At the bending area (FongYuan), the slip velocity reaches its maximum value of 3.35m/s. The slip is sustained for about 10 s, resulting in a 15.8 m dislocation. In sum, the slip rate at the northern part of the fault is vary large but the total duration time, less than 10 s, is relatively short compared to the duration of the subfaults at the southern part. The slip magnitude near the surface increases from south to north, with a local maximum near TsaoTun, then reaches the global maximum at northern bending region. This result is similar to field ground truth measurements [*Central Geological Survey*, 1999, 2000]. As the strike turns toward the east, both slip rate and accumulated slip decrease gradually. Note that the subfaults located

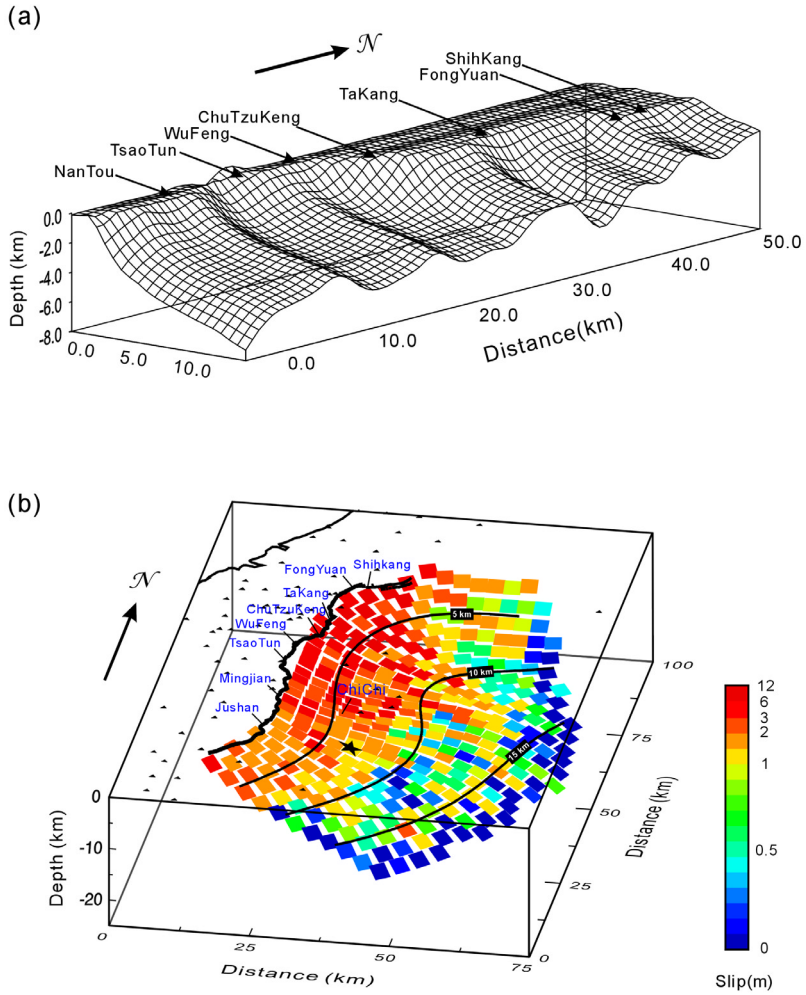

Figure 12. (a) Chinshui shale geometry from the seismic profile along the Chelungpu fault [*Wang et al.*, 2000]. (b) Perspective view of the 3-D trend surface fault plane with the inverted total slip distribution from the southern border. Solid lines indicated the surface break and isodepth line on the fault. Both Figures 12a and 12b show local towns along the surface break for comparison.

at the deeper part near the northern Puli basin also have large slip magnitude (i.e., subfault No.174, 227). The slip behavior in that area has a high slip rate, sustains for about 5–10 s then becomes quiet which is similar to the slip behavior at shallow bending area (subfault No. 73). This result points out that the shallow, and deeper large slips belong to the same rupture mechanism. Throughout the earthquake sequence, the rupture in this belted zone propagated from deeper to shallower sections, resulting in serious damage at the surface.

3.4. Rupture Velocity

[18] Under the assumption of multiple-time window, the rupture velocity can vary at a range equal or less than the initial value. If the slip begins at the first time window, the rupture at the subfault is earlier. Otherwise, if the rupture begins at the later window, its response delay time is larger at the subfault, and thus the rupture velocity is lower than the initial value. The greater the number of time windows the longer the duration time and the broader the range of rupture velocity can be detected. We assume 5.0 km/s as the

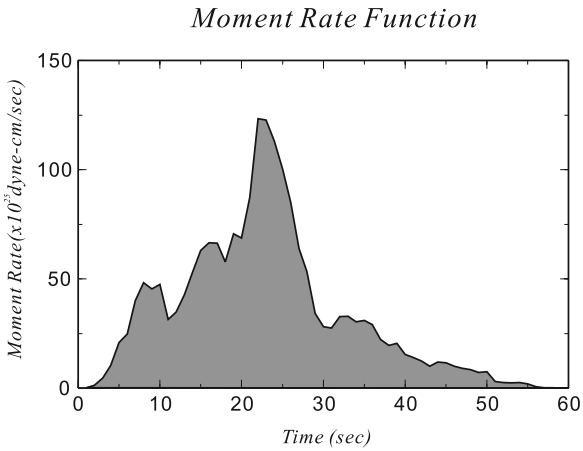

Figure 13. Moment rate function of the Chi-Chi earthquake. The moment rate unit used in the left axis is 10^{25} dyn cm/s.

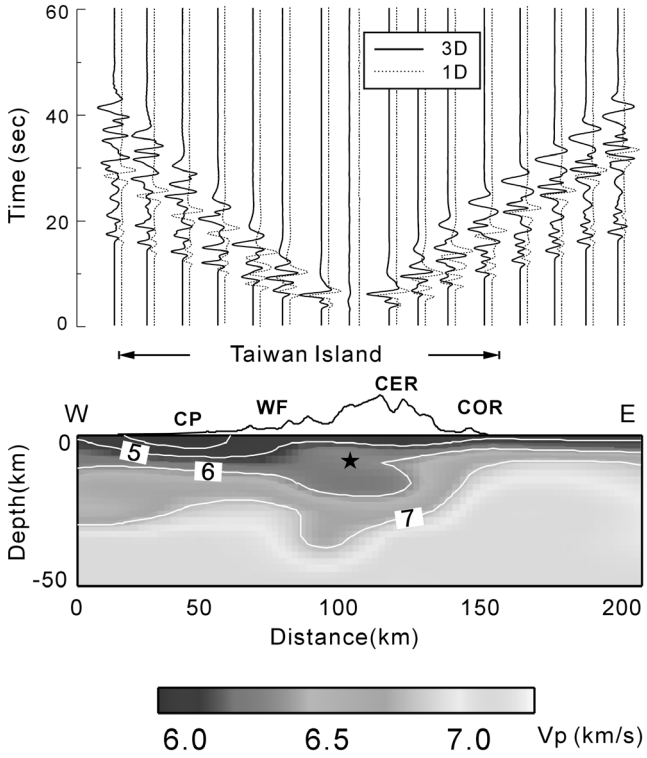

Figure A1. Synthetic waveforms along a west-east profile crossed the middle part of Taiwan. The comparison between 1-D (dotted lines) and 3-D (solid lines) synthetic are in vertical component velocity waveforms by an interval of every 10 km. The 3-D velocity model across the profile is shown at lower part, and the P wave velocity is presented by gray scale. The star indicates the location of the scenario earthquake. The surface topography (in a different scale) and main geological settings across the profile, including the Costal Plain (CP), Western Foothill (WF), Central Range (CER), and Costal Range (COR) are pointed out in the figure.

initial rupture velocity, and thus the maximum invertible rupture velocity on the fault plane can be constrained. Figure 9 shows the initial rupture delay time, inverted rupture delay time and inverted rupture velocity. To determine the real rupture delay time after the inversion, we consider the rupture front to have passed as the accumulated slip reach 0.1 m on the subfault. The shortest distance from the initial rupture point to the subfault divided by the inverted rupture delay time is the local rupture velocity. Results show that the inverted rupture delay time is different from the initial assumption. The rupture starts at the hypocenter and propagates outward with nonuniform rupture velocity and delay time. For depths shallower than the hypocenter, rupture velocity is faster than for the deeper subfault. This result indicates the initial rupture is propagating mainly from the shallower section of the fault. Rupture velocity near the surface break is more rapid, which may have been influenced by the free surface effect. Note that the rupture time is late at the deeper part of the fault, near the northern PuLi basin, by about 2–4 s and the rupture velocity in this area is relatively low. Here, the rupture may have encountered an asperity, requiring more time to overcome the resistance. This phenomenon is different from what has been inferred in previous rupture inversions [e.g., *Hisada*, 2001] and some models of dynamic rupture propagation. However, *Dalguer et al.* [2001] also suggested a slower rupture velocity at the northern part of the fault where the largest asperity occurred during the Chi-Chi earthquake. Thus the slower rupture velocity at the asperity derived from our inversion result is possible which is not completely opposite to the previous studies. The rupture velocity at asperities might have a set of limited variation and need to be careful examined.

[19] Using dense near field strong motion data with 48 time windows in the inversion, reoccurrence slip behavior along the fault plane has been revealed by this study. Although the determination of rupture velocity is difficult when the rupture is repeating, the results would, however, be nearer the natural phenomenon.

3.5. Risetime, Duration Time, and Maximum Slip Velocity

[20] Because the rupture at some subfaults exhibits repeated slip behavior, especially at the shallower part of the fault, we redefine the risetime, duration time, and maximum slip velocity as shown in Figure 10a. The redefined risetime, here, refers to the time when the slip rate reached the maximum value. Figure 10b shows the heterogeneous

Table 1. Inversion Parameters Compare With Other Studies[a]

Research	Data (Number)	Fault Model and Green's Functions	Seismic Moment, dyn cm	Maximum and Average Slip, m	Total Duration, s
Ma et al. [2001]	SM (21) + Tel (22) + GPS (131)	1-D (two segments) 1-D layer	4.6×10^{27}	14.0 –	28
Ji et al. [2001]	SM (36) + GPS (119)	1-D (three segments) 1-D layer	2.7×10^{27}	– –	–
Wu et al. [2001]	SM (47) + GPS (60)	1-D (three segments) 1-D layer	2.7×10^{27}	20.0 –	40
Zeng and Chen [2001]	SM (15) + GPS (130)	1-D (N segments[b]) 1-D layer	2.9×10^{27}	20.0 3.8	32
Chi et al. [2001]	SM (21)	1-D (1 segment) 1-D layer	4.1×10^{27}	23.0 –	30–35
This study	SM (103)	3-D (trend-surface) 3-D tomography	2.0×10^{27}	16.0 1.8	~60

[a]SM, strong motion data; Tel, teleseismic data, GPS, global position system data; dashes, no information in paper.
[b]Multiple segments with constant dip angle.

distribution of the risetime on the fault. There are longer risetimes near the hypocenter, but the subfaults close to the surface break are relatively short. Long risetimes are also found in the northern and southern parts of the fault, even if the total slip at these areas is negligible. Note that at the bending area where the maximum slip occurred, the risetime increases from the deeper section to the free surface. The total duration time in the study is redefined as the time from 10% cumulative slip to 90% cumulative slip (Figure 10b). Compared to the risetime, total duration time shows a simpler pattern. By using the depth of the hypocenter as a reference, the average time of the shallower part is about 20 s while the deeper part is less than 10 s. The total duration time for the maximum slip region arising from the northern PuLi basin is very short; only about 10 s. This area extends from the deeper section to the free surface. The last parameter is the maximum slip velocity at the subfault (Figure 10b). Owing to repeat slip, we only consider the maximum peak velocity during the whole slip time history. The slip velocity increases with epicenter distance along the mid depth of the fault plane, about 10–15 km. The average maximum slip velocity in this area is about 0.8 m/s. As the subfault approaches the north, the largest slip velocity increases and moves toward the ground surface. The maximum slip velocity on the whole fault plane is 3.35 m/s, located at the north bending region.

[21] Relations can be found after comparing risetime, duration time and maximum slip velocity. For the maximum slip region, located at the bend of the fault, both the risetime and duration time show shorter time periods but have larger maximum slip velocity. These results point out that the rupture reaches the maximum slip rate instantaneously then decays rapidly. Total rupture time in this region is only about 10 s. Around the hypocenter, there are different rupture behaviors at different depths. At the shallower section, the risetime is short but the duration time is longer. It shows that the slip velocity in this region rises quickly but decays slowly for a long time. The subfault at depth greater than the hypocenter shows a longer risetime but shorter duration time, indicating slip velocity reaches a maximum more slowly then quiets quickly. Note that near the surface break, just at the bending of the fault trace, both risetime and duration time are very long. At this area, the slip rate increases for a long time before reaching maximum slip velocity, followed by a long period of decay. This phenomenon indicates that the rupture behavior at local region is relatively complex.

4. Discussion

4.1. Compare With Aftershocks

[22] Figure 11 shows a comparison between inverted slip distribution and aftershocks. These aftershocks ($M_L > 1$) were recorded by CWB between 1999 September to 1999 November. There is a reasonable relationship between the two data sets. The area where large amounts of slip occur has fewer aftershocks. Most of the large magnitude aftershocks are located at the main shock slip ending edge. On the large slip area, almost all tectonic stress is released during the main shock, thus the probability of aftershock occurrence is reduced. Around the main shock slip edge, either background stress is not released completely by the main shock or stress transfer occurs due to the main shock. As a result, most of the large aftershocks occurred around the slipping edge. This phenomenon has been found in many source studies of damaging earthquakes, such as the 1992 Landers earthquake [*Wald and Heaton*, 1994] and the 1994 Northridge earthquake [*Wald et al.*, 1996].

4.2. Seismic Profile Versus Slip Area

[23] Results from rupture time history show that the rupture front is almost at a stop as it reached TsaoTun area. When considering the whole slip distribution, slip magnitude is relatively high in this area (Figure 12b). We determine the first asperity along the fault plane to be under TsaoTun. *Wang et al.* [2000] made a series seismic profile of the Chelungpu fault (Figure 12a); their results show an undulating fault surface along the south-north profile of the fault plane. A flat-and-ramp geometry between TsaoTun and Wu Fong is found which corresponds to the first asperity we obtain in the slip distribution. A similar relation is also found at the northern bend where the maximum slip region occurs. From the results of seismic profile, the depth of Chinshui shale after TsaoTun gradually becomes shallower along a low-angle dip then the fault plane quickly drops near Takang and follows a series of rises toward the surface. Compared to the rupture process, after the rupture overcomes the first asperity, it releases a large amount of rupture energy. Then the slip region rapidly extends toward the north and northeast. As the rupture front encounters this geometric resistance, the large slip turns to a northwest direction where the dip angle is gentler. This behavior is accompanied by the main tectonic stress, following a northwest-southeast direction, resulting in violent slip rupture behavior toward the surface. Although the slip distributed along the northeast part of the fault is relatively weak, it seems to separate from the main slip area. The initial rupture of this area starts from the east and develops toward the west, becoming concentrated at the bend in the fault. Slip direction in this area is not stable. From this observation, we hypothesize there might be a preexisting weak plane along which the rupture sequence tended to follow. Therefore the geometry of the whole fault system in the northern part of the trace is continuously changing.

[24] The results of the seismic reflection study show the complex geometry of the Chinshui shale. Although the fault model used in this study does not contain this high resolution, the results of the near field strong motion inversion are of better quality. It is therefore reasonable to infer that the

Figure B1. Resolution analysis under the assumption of input slip within four time windows. From left to right show (a) the true solution, (b) result inverted from 3-D Green's functions, and (c) result inverted from 1-D Green's functions. Both the slips in the individual time window and the final total slip are displayed for detailed comparison. The inverted slip distribution from the 1-D Green's functions is not acceptable. The total slip from 3-D Green's functions is slightly different from that of the actual model, about 99.8% recovered. The discrepancy between true model and the result from 1-D Green's functions is larger which is only 68.9% getting back.

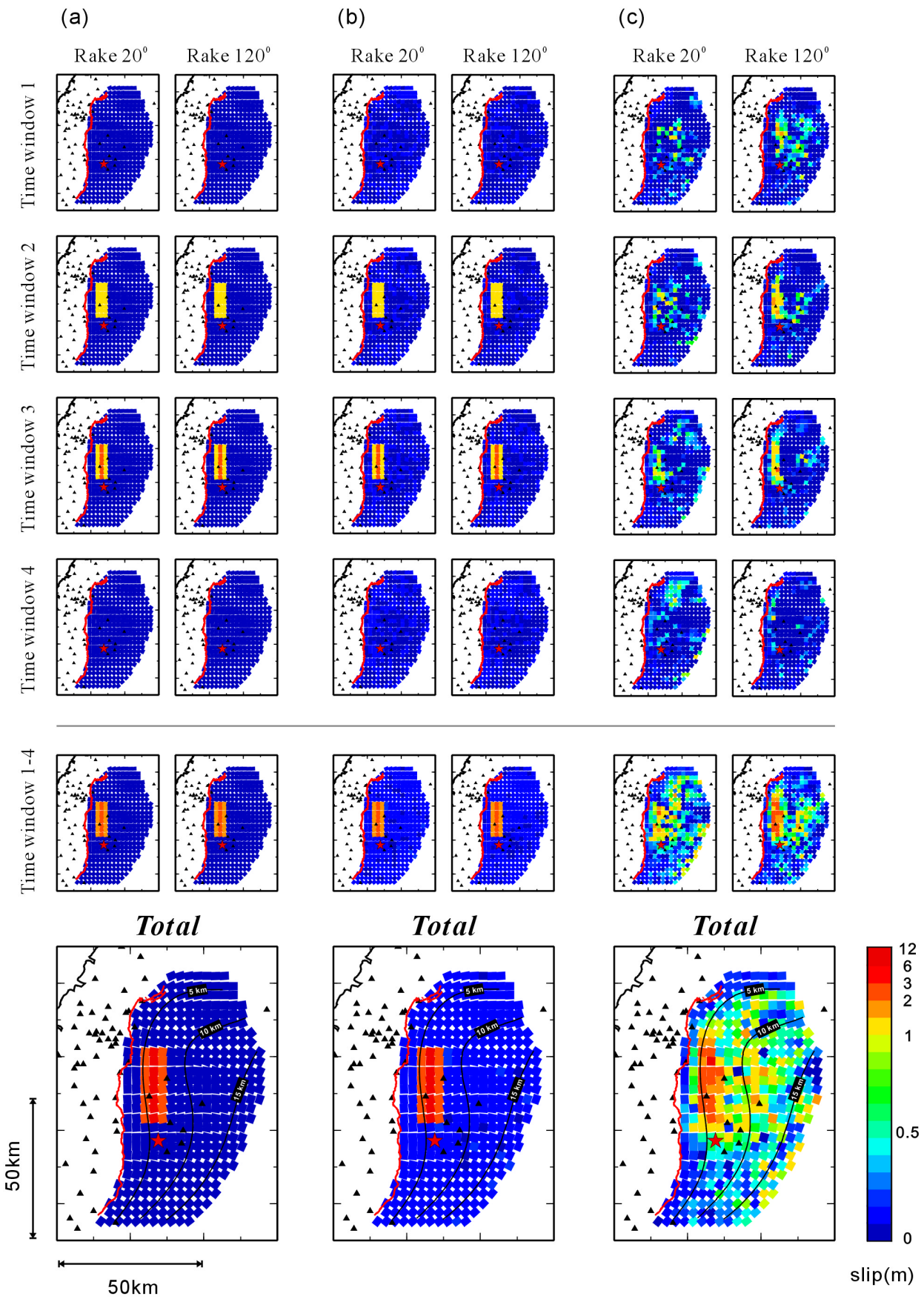
(a)
(b)
(c)
Rake 20°
Rake 120°
Time window 1
Time window 2
Time window 3
Time window 4
Time window 1-4
Total
5 km
10 km
15 km
50km
50km
12
6
3
2
1
0.5
0
slip(m)

Figure B1

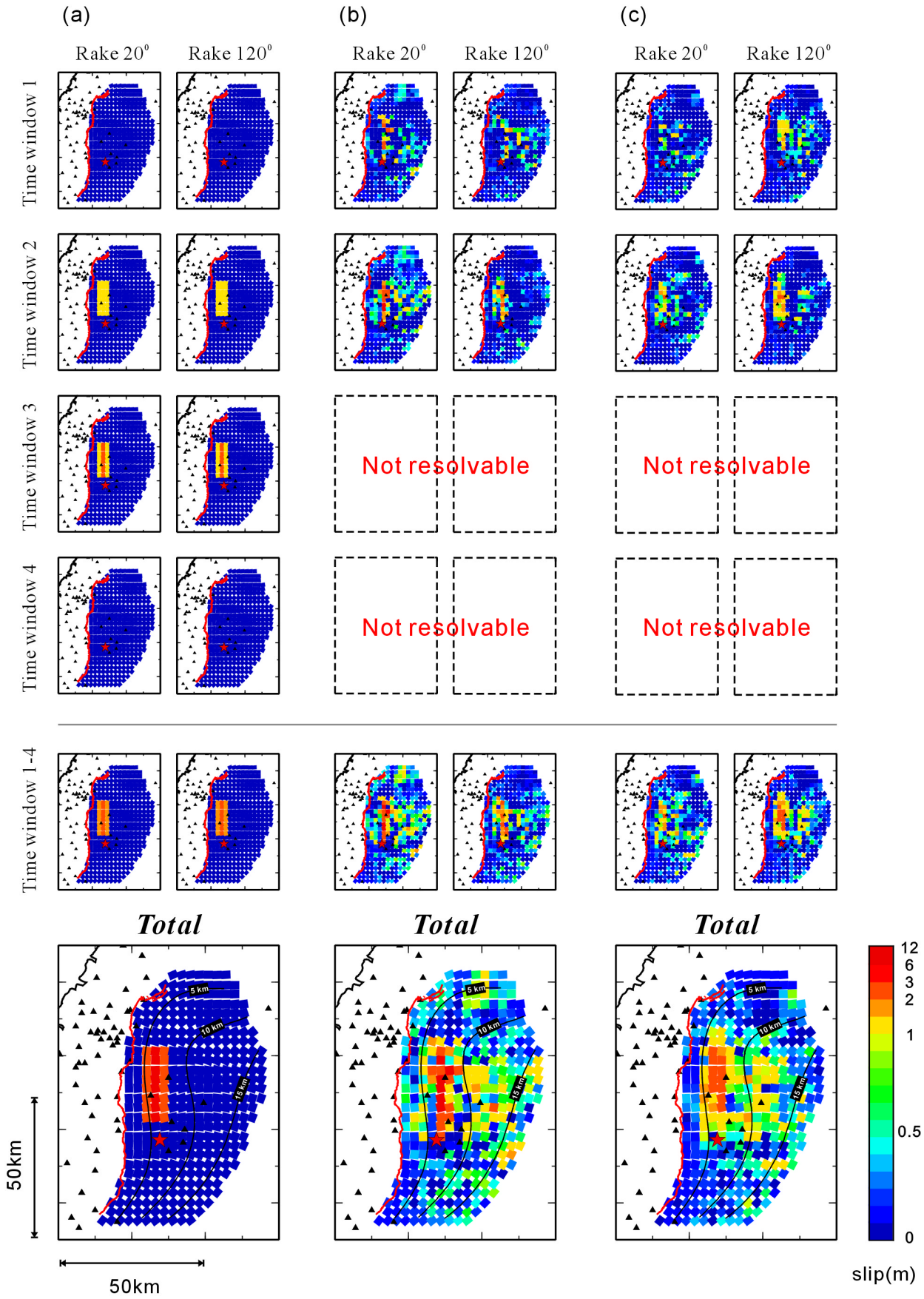
(a)
(b)
(c)
Rake 20°
Rake 120°
Time window 1
Time window 2
Time window 3
Time window 4
Not resolvable
Time window 1-4
Total
5 km
10 km
15 km
50km
50km
12
6
3
2
1
0.5
0
slip(m)

Figure B2

geometry of the Chelungpu fault is likely the primary control on the rupture behavior during the Chi-Chi earthquake.

4.3. Source Parameters

[25] The total seismic moment derived from this study is about 2.0×10^{27} dyn cm, which is near the final result from U.S. Geological Survey CMT (2.4×10^{27} dyn cm) and Earthquake Research Institute auto CMT (2.5×10^{27} dyn cm). Although this moment is smaller than the average value from earlier inversion results, the larger moments usually come from a simplified assumption of fault geometry [i.e., *Ma et al.*, 2001; *Chi et al.*, 2001]. For a more complex fault model with the combination of three or more segments, the inverted moments are decreased [*Zeng and Chen*, 2001; *Wu et al.*, 2001; *Ji et al.*, 2001]. Here, we applied a 3-D realistic fault model in this study, the moment obtained after the inversion is decreased again which is about 70–75% smaller than the multisegment fault models. From the inversion point of view, the closer to the realistic structure considered in the inversion (including the velocity and fault model), the fewer artificial slip patches occurred, and thus the smaller moment will be obtain after the inversion. A similar conclusion on the influence of how closed to the nature of the fault geometry and the inverted seismic moment is discussed by *Lee et al.* [2006]. It should also be kept in mind that the moment difference may have resulted from the different frequency band used in different data sets. Figure 13 shows the moment rate function of the Chi-Chi earthquake derived by summing all the source time functions of the subfault. It shows that the total rupture duration on the fault plane is near 1 minute, having the largest energy release during 20 to 26 s, quickly decaying then stopping at 60 s. The average focal mechanism of the subfault has 70% of the total slip, with a strike of 17°, a dip of 25° and a rake of 66°. Maximum slip is 15.8 m located near the northern bend in the fault trace, with a depth of 4.5 km. The average slip is 1.76 m, which is included the slipping subfault. The average risetime, duration time and slip velocity are 6 s, 14 s, and 0.5 m/s, respectively. Table 1 shows the parameters derived from this study. Also shown in Table 1 are the results from other studies for comparison.

5. Conclusion

[26] To ensure the highest possible resolution, a parallel nonnegative least squares inversion technique is used to invert the three-dimensional source rupture process of the 1999 Chi-Chi earthquake, Taiwan, determined from dense strong motion data. We take into account as many aspects as possible to improve the inversion result, including: (1) dense near field strong motion data that provided about a fivefold increase in the source region records available for the entire world. The total number of strong motion records used in this study is more than two times that of previous studies; (2) using a 3-D trend surface as the fault model to approximate recently revealed fault geometry; (3) comprehensive 3-D Green's functions are calculated to satisfy the complex 3-D velocity and improve the accuracy of source simulation; (4) taking into account the absolute timing for both Green's functions and observations; and (5) developing a parallel nonnegative least squares inversion to deal with the large number of time windows required to provide the highest possible resolution on source rupture process, including the rupture delay time, slip duration time and other source parameters. Our results indicate that the total duration of the Chi-Chi earthquake is about 60 s. Two large asperities are found during the rupture process. Most of the slip occurs at the shallower portion of the fault above the decollement, which is well defined by the 3-D fault model. Maximum slip is about 15.8 m located at the northern bend in the fault. This extreme large slip region extends toward to a depth of 15 km. The slip time history shows high complexity along the fault. In the south, slip repeats several times with low slip rate and long duration. While in the north, where slip is greatest, rupture behavior is dominated by mostly a single event with a high slip rate and a short duration of about 10 s. This high-resolution temporal-spatial slip distribution derived from the comprehensive 3-D Green's functions accounts for 3-D fault geometry provides a more accurate source rupture process to have a complete understanding of the kinematics of the Chi-Chi earthquake.

Appendix A: Synthetic Waveform Comparison Between 1-D and 3-D Velocity Model

[27] Figure A1 shows the synthetic waveform comparison between 1-D half-space model (Vp = 6.0 km/s, Vp = 3.46 km/s) and 3-D velocity model [*Rau and Wu*, 1995] along a west-east profile in middle Taiwan. The discrepancy between the waveforms is obvious. In west part, the 3-D synthetics show abundant surface waves and reflection phases. The traveltime of the main phases are slower than the result from half-space model. This is due to the low-velocity material under western coastal plain that cannot be represented in 1-D half-space or 1-D layered model. In eastern part, because of the collection of Philippine Sea plate that resulted in the high-velocity gradient under east coastal range, the 3-D synthetics show more high-frequency and earlier arrivals in the waveform compare to the 1-D synthetics. From this result, we know that the tectonic settings within Taiwan would have an evident influence on seismic wave propagation in both traveltime and waveform. The complexities of 3-D continental structure cannot be ignored and is necessary to be considered in the Green's functions for the inversion study.

Appendix B: Resolution Tests on 1-D and 3-D Green's Functions and the Necessity of Extra Multiple-time Window

[28] To examine the influence between 1-D and 3-D Green's functions and the necessity of extra time window

Figure B2. Resolution analysis. The inputted true model is the same but inverted by only two time windows. From left to right show (a) the true solution, (b) result inverted from 3-D Green's functions, and (c) result inverted from 1-D Green's functions. With limited time window, the inverted slip distributions from 1-D and 3-D Green's functions are not acceptable. The inverted total slip from 3-D Green's functions is about 60.6% recovered. The discrepancy between true model and the result from 1-D Green's functions is even large with only 51.4% recovered.

for the longer source duration time, we conducted a resolution analysis by generating a set of slip distributions which we inverted for the same 3-D fault geometries with different 1-D and 3-D Green's functions. To clarify the problems, we rather consider the total 48 time windows used in the inversion than simplified the input dislocation patch in this investigation. Results can be generalized to extra multiple-time window. The input slip has a 1.0 m pattern at secondary time window (second second after the assumed rupture front pass through) and a 2.0 m surrounded by 1.0 m pattern at third time window (third second after the passage of rupture front). The slips arise along two components, rake 20° and rake 120°, located at the middle part of the fault. The rupture velocity in the input model is assumed as a constant 2.5 km/s. First, we give the same number of time window as in the input model and invert by 1-D (from 1-D layer model [*Ho and Shin*, 1994] and 3-D (tomography model from *Rau and Wu* [1995]) Green's functions with initial rupture velocity 2.5 km/s. The second test apply a fewer time window compare to the input model to examine the necessary of extra time window. The smooth and minimum solution constraints are not considered in these tests. We then compared the imaged dislocations to identify the necessary of extra multiple-time window and the tradeoffs involved in 1-D and 3-D Green's functions.

[29] Figure B1 compares the slip distributions of the true model with those obtained from the 1-D and 3-D Green's functions. The slips in true solutions arise in different time window as shown in Figure B2a. For the inverted results using full 3-D Green's functions (Figure B1b), the pattern and amplitude in the imaged slip distribution is perfectly match with the input model. True that there are some small slip amplitudes of less than 0.2 m appear in both the rake 20° and rake 120° components on the fault plane, but this has no significant influence on overall slip distribution. Figure B1c shows the imaged slip distribution invert from 1-D Green's functions. The inverted slip is evidently much sparser than that in the true model, and the estimated slip is separated within all four time windows. In addition, a significant number of pseudoslip patches are distributed in the bottom portion near the northern corner of the fault which is dominated by the rake 120° component. The finding of such inversion artifacts generated by the 1-D Green's functions is similar with the result of previous inversion studies [*Ma et al.*, 2001; *Zeng and Chen*, 2001; *Wu et al.*, 2001; *Ji et al.*, 2001] which need an independent deep asperity at the north part of the fault to explain the observations. This is highly possible to be due to the 1-D Green's functions provide incorrect traveltime and waveform information and then mapping back into the source. The inversion try to use incorrect timing information in the Green's functions to explain the input data then resulted in artificial slip on the fault plane. The total slip combined from all four time windows are also shown in the lower part of Figure B1. The inverted total slip from 3-D Green's functions is slightly different from that of the actual model, about 99.8% recovered. The discrepancy between true model and the result from 1-D Green's functions is larger which is only 68.9% recovered.

[30] Subsequently, we used a similar approach to test the need of extra time window in the inversion. Figure B2 compares the slip distributions of the true model (four time windows) with those obtained from the 1-D and 3-D Green's functions inverted by limited, i.e., two, time windows. The inverted slip image on both the 3-D and 1-D Green's functions has a sparser dislocation compare to the known solution. The main location of the slip patch inverted from 3-D Green's functions is consistent with the actual solution while the result inverted from 1-D Green's functions is located broader. From the total slip patterns, both results show clear inverted artifact slips exist in deeper portions (>10 km) and have an amplitude value of larger than 1 m. This is due to not enough time-space resolvable parameters provide in the inversion to explain the later slips, and thus try to use the farther locations (with longer rupture delay time) to explain the input data. With the limited time window, both the inverted images from 1-D and 3-D Green's functions are by far worse, and the findings, in fact, provide solid evidence that inversion with extra multiple-time window is necessary for Chi-Chi earthquake records.

[31] Comparing the inverted total slip distributions, as shown in Figures B1 and B2, it is apparent that an accurate description of Green's functions, especially when the known tectonic settings are complex, may considerably affect the inversion results. In addition, the synthetic tests suggest that when 1-D Green's functions are used, the estimated slip in the northern deeper portion is less reliable on account of inaccuracies in the path effect. Furthermore, from our time window analyses, we believe that the extra multiple-time window analysis which gives extra free parameters is stable and necessary, while the more time windows give us the ability to explain most of the recorded information. Bearing these findings in mind, we reach the conclusion that, most assuredly, both the extra time windows and an accurate description of 3-D Green's functions are necessary and even crucial when attempting to obtain reliable results with regard to the location and amplitude of slips.

[32] **Acknowledgments.** The authors thank the Central Weather Bureau for providing TSMIP data used in this study. We would also like to thank Ta-Liang Teng for detailed and critical reviews. Special thanks go to IESAS and the Seismological Lab at Caltech where many valuable discussions occurred. Much of this work was done while the author was a Ph.D. student of the Institute of Geophysics, NCU. This research was supported by National Science Council, Taiwan, under NSC89-2921-M-008-012-EAF and IESAS1145.

References

Central Geological Survey (1999), Geological survey report for September 21 earthquake (in Chinese), 315 pp., Central Geol. Surv., Minist. of Econ. Affairs, Taipei, Taiwan.

Central Geological Survey (2000), Special issue for the Chi-Chi earthquake, 1999 (in Chinese), 272 pp., Central Geol. Surv., Minist. of Econ. Affairs, Taipei, Taiwan.

Cerjan, C., D. Kosloff, R. Kosloff, and M. Reshef (1985), A nonreflecting boundary condition for discrete acoustic and elastic wave equations, *Geophysics*, *50*, 705–708.

Chi, W. C., D. Dreger, and A. Kaverina (2001), Finite-source modeling of the 1999 Taiwan (Chi-Chi) earthquake derived from a dense strong-motion network, *Bull. Seismol. Soc. Am.*, *91*, 1144–1157.

Clayton, R. W., and B. Engquist (1977), Absorbing boundary conditions for acoustic and elastic wave equations, *Bull. Seismol. Soc. Am.*, *6*, 1529–1540.

Dalguer, L. A., K. Irikura, J. Riera, and H. C. Chiu (2001), The importance of the dynamic source effects on strong ground motion during the 1999 Chi-Chi, Taiwan, earthquake: Brief interpretation of the damage distribution on buildings, *Bull. Seismol. Soc. Am.*, *95*, 1112–1127.

Gropp, W., E. Lusk, N. Doss, and A. Skjellum (1996), A high-performance, portable implementation of the MPI message passing interface standard, *Parallel Comput.*, *22*(6), 789–828.

Hartzell, S. H., and T. H. Heaton (1983), Inversion of strong ground motion and teleseismic waveform data for the fault rupture history of the 1979 Imperial Valley, California earthquake, *Bull. Seismol. Soc. Am.*, *73*, 1553–1583.

Hisada, Y. (2001), A theoretical omega-square model considering the spatial variation in slip and rupture velocity. part 2: Case for a two-dimensional source 16 model, *Bull. Seismol. Soc. Am.*, *91*, 651–666.

Ho, M. Y., and T. C. Shin (1994), 3-D velocity structure of western Taiwan, *Meteorol. Bull.*, *40*, 216–234.

Ji, C., D. V. Helmberger, T.-R. Song, K.-F. Ma, and D. J. Wald (2001), Slip distribution and tectonic implication of the 1999 Chi-Chi, Taiwan, earthquake, *Geophys. Res. Lett.*, *28*(23), 4379–4382.

Lee, C. T., C. T. Cheng, C. W. Liao, and Y. B. Tsai (2001), Site classification of Taiwan free-field strong motion stations, *Bull. Seismol. Soc. Am.*, *91*, 1283–1297.

Lee, K. S., and H. W. Chen (2000), Evaluate of the three-dimensional velocity structure in Taiwan region, paper presented at Geophysical Annual Meeting, Chin. Geophys. Soc., Taipei, Taiwan.

Lee, S. J., and K. F. Ma (2000), Rupture process of the 1999 Chi-Chi, Taiwan, earthquake from the inversion of teleseismic data, *Terr. Atmos. Oceanic Sci.*, *11*, 591–608.

Lee, S. J., K. F. Ma, and H. W. Chen (2006), Effect of fault geometry and slip style on near-fault static displacements caused by the 1999 Chi-Chi, Taiwan, earthquake, *Earth Planet. Sci. Lett.*, *241*, 336–350.

Ma, K. F., J. H. Wang, and D. Zhao (1996), Three-dimensional seismic velocity structure of the crust and uppermost mantle beneath Taiwan, *J. Phys. Earth*, *44*, 85–105.

Ma, K. F., C. T. Lee, Y. B. Tsai, T.-C. Shin, and J. Mori (1999), The Chi-Chi Taiwan earthquake: Large surface displacements on an inland thrust fault, *Eos Trans. AGU*, *80*, 605, 611.

Ma, K. F., J. Mori, S. J. Lee, and S. B. Yu (2001), Spatial and temporal distribution of slip for the 1999 Chi-Chi, Taiwan, earthquake, *Bull. Seismol. Soc. Am.*, *91*, 1069–1087.

Rau, R. J., and F. T. Wu (1995), Tomographic imaging of lithospheric structures under Taiwan, *Earth Planet. Sci. Lett.*, *135*, 517–532.

Roecker, S. W. (1987), Three-dimensional P and S wave velocity structures beneath Taiwan: Deep structure beneath an arc-continent collision, *J. Geophys. Res.*, *92*, 10,547–10,570.

Wald, D. J., and T. H. Heaton (1994), Spatial and temporal distribution of slip for the 1992 Landers, California earthquake, *Bull. Seismol. Soc. Am.*, *84*, 668–691.

Wald, D. J., D. V. Helmberger, and T. H. Heaton (1991), Rupture model of the 1989 Loma Prieta earthquake from the inversion of strong-motion and broadband teleseismic data, *Bull. Seismol. Soc. Am.*, *81*, 1540–1572.

Wald, D. V., T. H. Heaton, and K. W. Hudnut (1996), Slip history of the 1994 Northridge, California, earthquake determined from strong-motion, teleseismic, GPS, and leveling data, *Bull. Seismol. Soc. Am.*, *86*, s49–s70.

Wang, C. Y., C. H. Chang, and H. Y. Yen (2000), An interpretation of the 1999 Chi-Chi earthquake in Taiwan based on the thin-skinned thrust model, *Terr. Atmos. Oceanic Sci.*, *11*, 609–630.

Wu, C., M. Takeo, and S. Ide (2001), Source process of the Chi-Chi earthquake: A joint inversion of strong motion data and global positioning system data with a multifault model, *Bull. Seismol. Soc. Am.*, *91*, 1128–1143.

Yu, S. B., et al. (2000), Preseismic deformation and coseismic displacements associated with the 1999 Chi-Chi, Taiwan earthquake, *Bull. Seismol. Soc. Am.*, *91*, 995–1012.

Zeng, Y., and C. H. Chen (2001), Fault rupture process of the 20 September 1999 Chi-Chi, Taiwan, earthquake, *Bull. Seismol. Soc. Am.*, *91*, 1088–1098.

H.-W. Chen and K.-F. Ma, Institute of Geophysics, National Central University, Jung-Li 320, Taiwan. (hwchen@earth.ncu.edu.tw; fong@earth.ncu.edu.tw)

S.-J. Lee, Institute of Earth Sciences, Academia Sinica, Nankang, Taipei 115, Taiwan. (sjlee@earth.sinica.edu.tw)